TECHNISCHE UNIVERSITÄT DRESDEN

High Resolution Optical Tweezers Optimized for Biological Studies

D I S S E R T A T I O N

zur Erlangung des akademischen Grades

Doctor rerum naturalium

(Dr. rer. nat.)

vorgelegt

der Fakultät Mathematik und Naturwissenschaften

der Technischen Universität Dresden

von

Mohammed Mahamdeh

Dresden, June 2011

High Resolution Optical Tweezers for Biological Studies
Mohammed Mahamdeh, PhD thesis, TU-Dresden, June 2011.

Supervisor:

Dr. Erik Schäffer

Nanomechanics group, Biotechnology Center (BIOTEC),TU-Dresden
Tatzberg 47-51, 01307 Dresden, Germany

Thesis Advisory Committee:

Prof. Jonathon Howard

Max Planck Institute of Molecular Cell Biology and Genetics (MPI-CBG)
Pfotenhauerstrasse 108, 01307 Dresden, Germany

Prof. Dr. Frank Jülicher

Max Planck Institute for the Physics of Complex Systems (MPI-PKS)
Nöthnitzer strasse 38, 01187 Dresden, Germany

This thesis was reviewed by:

Prof. Jonathon Howard
Prof. Dr. Petra Schwille

The work described in this thesis was performed at the Nanomechanics group, Biotechnology Center (BIOTEC), TU-Dresden, Tatzberg 47-51, 01307 Dresden, Germany

The author was enrolled in the PhD program of Dresden International Graduate School for Biomedicine and Bioengineering.

The author was supported by the Deutsche Forschungsgemeinschaft (Emmy Noether Grant; Erik Schäffer).

To my family ...

Declaration

Declaration according to §5.5 of the doctorate regulations

I herewith declare that I have produced this paper without the prohibited assistance of third parties and without making use of aids other than those specified; notions taken over directly or indirectly from other sources have been identified as such. This paper has not previously been presented in identical or similar form to any other German or foreign examination board

The thesis work was conducted from May 1,2007 to May 1, 2011 under the supervision of Dr. Erik Schäffer at the Biotechnology Center (BIOTEC) of the Technische Universität Dresden.

I declare that I have not undertaken any previous unsuccessful doctorate proceedings.

I declare that I recognize the doctorate regulations of the *Fakultät für Mathematik und Naturwissenschaften* of the *Technische Universität* Dresden.

Mohammed Mahamdeh
Dresden, June 1, 2011

Summary

In the past decades, numerous single-molecule techniques have been developed to investigate individual bio-molecules and cellular machines. While a lot is known about the structure, localization, and interaction partners of such molecules, much less is known about their mechanical properties. To investigate the weak, non-covalent interactions that give rise to the mechanics of and between proteins, an instrument capable of resolving sub-nanometer displacements and piconewton forces is necessary. One of the most prominent biophysical tool with such capabilities is an optical tweezers.

Optical tweezers is a non-invasive all-optical technique in which typically a dielectric microsphere is held by a tightly focused laser beam. This microsphere acts like a microscopic, three-dimensional spring and is used as a handle to study the biological molecule of interest. By interferometric detection methods, the resolution of optical tweezers can be in the picometer range on millisecond time scales. However, on a time scale of seconds—at which many biological reactions take place—instrumental noise such as thermal drift often limits the resolution to a few nanometers. Such a resolution is insufficient to resolve, for example, the ångstrom-level, stepwise translocation of DNA-binding enzymes corresponding to distances between single base-pairs of their substrate. To reduce drift and noise, differential measurements, feedback-based drift stabilization techniques, and 'levitated' experiments have been developed. Such methods have the drawback of complicated and expensive experimental equipment often coupled to a reduced throughput of experiments due to a complex and serial assembly of the molecular components of the experiments.

We developed a high-resolution optical tweezers apparatus capable of resolving distances on the ångstrom-level over a time range of milliseconds to 10s of seconds in surface-coupled assays. Surface-coupled assays allow for a higher throughput because the molecular components are assembled in a parallel fashion on many probes. The high resolution was a collective result of a number of simple, easy-to-implement, and cost-efficient noise reduction solutions. In particular, we reduced thermal drift by implementing a temperature feedback system with millikelvin precision—a convenient solution for biological experiments since it minimizes drift in addition to enabling the control and stabilization of the experiment's temperature. Furthermore, we found that expanding the laser beam to a size smaller than the objective's exit pupil optimized the amount of laser power utilized in generating the trapping forces. With lower powers, biological samples are less susceptible to photo-damage or, vice versa, with the same laser power, higher trapping forces can be achieved. With motorized and automated procedures, our instrument is optimized for high-resolution, high-throughput surface-coupled experiments probing the mechanics of individual biomolecules. In the future, the combination of this setup with single-molecule fluorescence, super-resolution microscopy or torque detection will open up new possibilities for investigating the nanomechanics of biomolecules.

Contents

Chapter 1

Introduction

1.1 History of optical tweezers

It all started with a simple calculation made by Arthur Ashkin [1]:

> My interest in the subject was aroused in 1969 by the following "back of the envelope" calculation of the magnitude of the radiation pressure force of light on a totally reflecting mirror.

Ashkin calculated that 1 W of laser would exert a nanonewton radiation force on the mirror with virtually no effect compared to macroscopic forces. If the same force is exerted on a small micrometer sized particle, the particle should accelerate and it would be possible to measure the radiation pressure, which he did experimentally in 1970 [2]. In that seminal work, latex dielectric microspheres, once in the vicinity of a mildly focused Gaussian laser beam, were drawn to the beam's center then accelerated in the direction of laser propagation. While acceleration of the microspheres was expected and is explained by scattering, the attraction to the beam center was not expected. Ashkin showed that the attraction is due to the intensity gradient of the laser and that its direction depended on the refractive index of the microsphere relative to the medium. He treated the microspheres as lenses and calculated the scattering and the attraction force—which he named the gradient force—using geometrical optics and found good agreement with measurements.

Understanding the scattering and gradient forces inspired forming the first three dimensional (3D) optical trap using two counter propagating laser beams ([2], Fig. 1.1a).

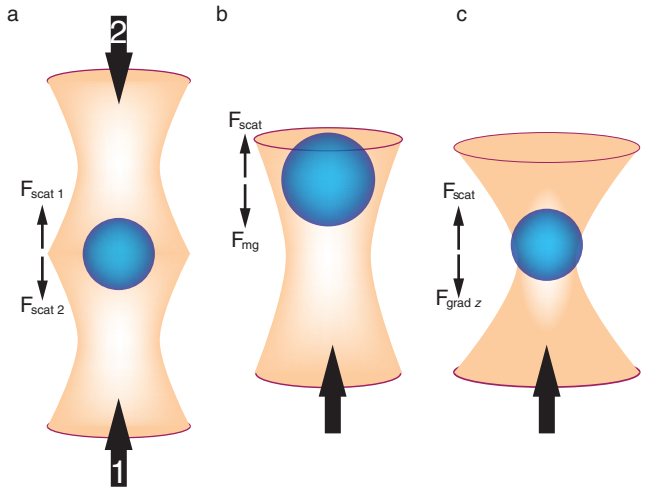

FIGURE 1.1 OPTICAL TRAPS - (a) Counter propagating, (b) levitation and (c) single beam optical traps. Stable axial trapping results from a balance between the counteracting axial forces on the microsphere. The axial forces acting on the microsphere are: the scattering force (F_{scat}), the gravitational force (F_{mg}), and the axial gradient force (F_{gradz}) for a, b, and c respectively. Thick arrows point to the direction of laser propagation.

The microspheres were confined laterally by the gradient forces and axially by the balance of the scattering forces of the two beams. Blocking one beam accelerated the microspheres in the direction of the other, thus, establishing a guide-and-sort application. Within one year, Ashkin introduced another trap where the axial scattering of a vertically propagating beam is counteracted by the gravitational forces of the microsphere ([3], Fig. 1.1b). Using the so called levitation trap, it was possible to levitate 20 μm glass spheres and stably trap them in air for hours.

For the following years, optical trapping was mainly used not to trap dielectric microspheres but for atom trapping, cooling and atom optics. The scientific success in that field granted Steven Chu—a colleague of Ashkin—the Nobel prize in 1997.

The real start for optical trapping to expand into other fields of science was in 1986 when Ashkin and coworkers introduced yet another type of optical traps known today as "optical tweezers" ([4], Fig. 1.1c). In optical tweezers, a laser beam is tightly focused by a high numerical aperture (NA) objective into a diffraction limited spot. Unlike the previous traps that needed an external force to stabilize the trap (i.e. scattering and the gravitational force), optical tweezers stabilization is intrinsic. The intensity gradient in the axial direction (the direction of laser propagation) is large enough that the axial

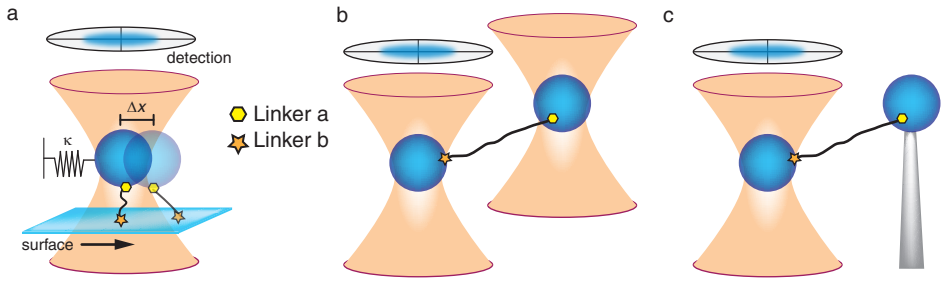

FIGURE 1.2 COMMON CONFIGURATION FOR BIOLOGICAL MEASUREMENTS - (a) The molecule under examination is biochemically connected to the surface of a flow cell from one side and to a trapped microsphere from the other side. For illustration purposes the microsphere is connected to a spring resembling the optical tweezers. Displacements of the microsphere generate forces that stretch the molecule. Instead of the surface, the molecule can be tethered to another microsphere: (b) held in another trap; dual trap configuration or (c) held by a micropipette

gradient force is larger than the scattering force. Thus, the axial gradient counteracts the scattering forces and stabilizes the trap. Since then and to the present day, optical tweezers are used in a wide spectrum of research fields. For example, in characterizing biomolecules and measuring their dynamics [5, 6], in colloidal physics [7] and in optical manipulations of aerosols [8], to name some.

1.2 Optical tweezers in biology

The first application of optical tweezers in biological studies was the trapping of Tobacco mosaic virus (TMV) and bacteria using an Argon laser ($\lambda = 514\,\text{nm}$) [9]. Using a visible laser was highly damaging to the trapped bacteria due to its high absorbance in the visible range which heated the bacteria to death. To avoid this optical damage—know as opticution—an infrared (IR) laser was used for trapping since biological matter is fairly transparent to IR light. Trapped yeast were able to divide and multiply with apparently no damage [10]. This bio-friendly trapping combined with piconewton and nanometer sensitivity is ideal for biological studies. Within the past two decades optical tweezers were used in a variety of biological experiments both *in vivo* and *in vitro* with a scale ranging from cells down to single biomolecules. For example, they were used for cell sorting and cell surgery [11], for measuring the mechanics of molecular motors of the cytoskeleton including step sizes and stalling forces [12, 13], protein friction [14], and for characterizing DNA and RNA as well as their related enzymes such as DNA(RNA)

polymerases [15, 16, 17].

It should be mentioned that in standard quantitative measurements, the molecule of interest in not directly probed. Instead, a dielectric microsphere—serving as a handle and a probe—is trapped and the target molecule is biochemically connected to it. This is convenient as most biomolecules cannot be stably trapped. In addition, microspheres are easier to calibrate than biomolecules. A common configuration is to tether the molecule to the microsphere from one side and to a reference point from the other side. For example, in studying the mechanics of DNA, a double stranded DNA (dsDNA) was tethered between a trapped microsphere and a flow cell surface. By moving the surface it was possible to stretch the DNA molecule which in response exerted a force on the microsphere and displaced it from the trap center ([18], Fig. 1.2a). In other experiments the tethered molecules interacts with a partner immobilized elsewhere as in studies of molecular motors of the cytoskeleton. Other than a cover slip surface, a reference can be another microsphere held by another trap or by a micropipette (Fig. 1.2b,c).

1.3 Measuring forces and displacements with optical tweezers

Optical tweezers can exert and measure forces in the sub-piconewton range and measure displacements in the sub-nanometer range. For small displacements, optical tweezers are a Hookian spring; displacements of trapped particles from the center of the trap is opposed by a restoring force proportional to the displacement, $F = \kappa \Delta x$. To measure the force, the force constant of the trap (the trap stiffness, κ) and the displacement (Δx) need to be known.

Position detection of the microsphere is possible by a number of methods. Video imaging is the simplest virtually requiring no changes to the setup. Its spatial and temporal resolution are determined by the pixel size and the acquisition rate respectively. The standard detection method used in optical tweezers is the back-focal-plane detection in which the interference of the light scattered from the microsphere with the unscattered light is measured [19]. The interference pattern in the back focal plane, hence the name, is detected and monitored, usually by a silicon based quadrant photodiode (QPD). Back-focal-plane detection offers, in principle, sub-ångstrom and microseconds resolution in all three dimensions. Likewise, a number of methods can be used for calibrating the trap stiffness. Each method has it advantages and drawbacks. To avoid unnecessary

repetition, an overview of common calibration methods in addition to the method we are using is presented Chapter 3.

The capabilities of an optical tweezers setup are defined by its resolution and accuracy. Resolution depends on the detection method and is limited by noise on the measurements. Accuracy depends on the calibration method. Since its introduction, optical tweezers are under a continuous improvement and optimization process to achieve the highest resolution and accuracy. Nowadays, nanometer and millisecond resolution are readily achievable in optical tweezers setups, but is that enough?

The needed resolution depends greatly on the investigated system. For example, the molecular motor kinesin carries a cargo and move along microtubules with a step size of 8 nm [12]. A spatial resolution of a nanometer is sufficient for measuring its steps. On the other hand, a DNA molecular motor like RNA polymerase takes steps of one nucleotide, that is 3.4 Å. Thus, ångstrom resolution is needed to resolve such steps. Besides resolving steps, higher temporal resolution makes it possible to measure the dwell time between two steps of the motor which gives insights into its kinetics. In general, many of the mechanical movements in the cell are on the ångstrom level. The ability to observe such movements will open a yet to be discovered area of biomolecule mechanics.

1.4 High resolution optical tweezers

In traditional optical tweezers experiments (Fig. 1.2a) sub-nanometer resolution is hard to access due to noise. Noise in optical tweezers stems from (i) the instrument and environment, and (ii) the Brownian motion. Brownian noise is a fundamental limit caused by thermal fluctuations; a trapped microsphere is continuously bombarded by thermally driven molecules of the surrounding medium (typically water). As a result the microsphere is in a continuous motion around its equilibrium position.

Although unavoidable, Brownian noise can be reduced by averaging and by tuning experimental parameters. Lowering the origin of the fluctuations, the temperature, is intuitive but has a weak effect because the range of temperature in biological experiments is a small fraction of the absolute temperature. Using small microsphere reduces the drag coefficient allowing the microsphere to fluctuate faster than larger microspheres thus distributing the noise over a larger bandwidth. Also, averaging helps to reduce the

Brownian noise since it is a random process and has a time average of zero. Averaging improves spatial resolution on the expense of the temporal resolution, so a compromise need to be made depending on the experiment [20, 21].

Instrumental and environmental noise is the other type that limits the resolution. It includes intrinsic noise of the different components of the setup and the noise coupled into the setup from the surroundings such as mechanical and acoustical vibrations, and electrical noise. These noise types are common for all optical tweezers and there are common measures recommended for reducing them. A description of each type and how it is reduced in our setup can be found in Chapter 3.

Taking the aforementioned into consideration it was possible to observe 5 Å at 1 Hz stepping rate when the setup had the chance to equilibrate overnight [22]. Maintaining this resolution was compromised by thermal disturbances in the setup during every day use. Thermal drift was the most sever noise resulting in a drift as high as 2μm/min. To reduce thermal drift, we introduced a simple temperature feedback system able of restoring thermal equilibrium within 100 seconds after a disturbance. With such a system, we were able to maintain a base-pair resolution in our setup (Chapter 5). Other solutions for maintaining high resolution include using a feedback system to track a fiducial marker on the surface of the flow cell that compensates mechanical noise [23]. Also, decoupling the assay from the surface as in Fig. 1.2 proved to improve the resolution not only because it isolated the assay from the experimental noise but also because–although counter intuitive—a dual trap assay experience lower Brownian noise than a single trap [21].

Interestingly, within this work, we found that—as a side effect—under-filling the trapping objective could reduce thermal drift effects. Expanding the trapping laser to sizes slightly larger than the exit pupil of the trapping objective is common in optical tweezers [24]. It is supposed to improve the axial trap efficiency as found in theoretical studies based on ray optics. Motivated by the lack of both the experimental work and a more exact theoretical treatment, we addressed the question of what the optimal ratio of the trapping beam width to the objective exit pupil is. We found that slightly under-filling the pupil optimized the trap efficiency for all directions. The exact ratio depended laterally on the microsphere size while axially it was rather constant (Chapter 4).

After this introduction, the rest of the thesis is organized in the following way:

- Chapter 2 is an overview of the physics of optical trapping. A simple model describing the optical trapping is presented followed by a summary of the theoretical models and the equations used for calculations of the trapping forces.

- Chapter 3 firstly discusses noise types on the optical tweezers and the solutions used to reduce each type. The high resolution of the setup is demonstrated by resolving steps of the size of a DNA base-pair. The second part of the chapter is a detailed description of our optical tweezers; its design, components, and how it is operated.

- Chapter 4 focuses on optimizing the trapping efficiency with respect to the filling ratio of the trapping objective. The trap stiffness was measured as a function of the filling ratio and the microsphere radius. The results were supported by theoretical calculations. Finally, conclusions and recommendations are presented.

- Chapter 5 addresses the reduction of the thermal drift noise using a temperature feedback solution. The design and implementation of the feedback is explained and its performance at different configurations is measured. The feedback restored thermal equilibrium and preserved the base-pair resolution of the setup.

- Chapter 6 summarizes the results and presents the conclusions drawn from the results. The chapter ends with an outlook for further improvements of the setup.

- The appendix is a step-by-step protocol for building high-resolution optical tweezers. Suggestions for control measurements, generic notes and precautions are included in the protocol. Parts of the protocol are generic and applicable to other optical tweezers while other parts are specific for our setup.

Chapter 2

Physics of optical tweezers

How is a microsphere trapped? What are the gradient and scattering forces and how do you calculate them? These are the question of interest in this chapter. The presented descriptions and calculations are relevant to dielectric microspheres, i.e. non-absorbing and non-magnetic ones, since they are the standard probes for force and displacement measurements in optical tweezers.

2.1 Trapping forces on dielectric microspheres

To understand how a dielectric microsphere is trapped in an optical tweezers it is better to refer to a simple qualitative description illuminating how trapping forces are generated. Based on ray (geometric) optics, the focused laser is composed of a bundle of rays (Fig. 2.1). Each ray has a momentum proportional to its intensity. Once at the interface between the medium and the microsphere, a ray is reflected and refracted according to Snell's low, $n_m \sin\theta_i = n_p \sin\theta_r$, where n_m is the refractive index of the medium, θ_i is the incidence angle, n_p is the refractive index of the microsphere, θ_r is the refraction angle. Due to diffraction the ray changes direction, thus its momentum changes resulting in an equal and opposite change in the microspheres momentum. The net momentum change of all rays results in a force pointing towards the center of the focus, the *gradient force*. On the other hand, the momentum change caused by reflection results in a net *scattering force* pushing the microsphere out from the focus in the direction of the light propagation. The microsphere is stably trapped if the gradient force is larger than the

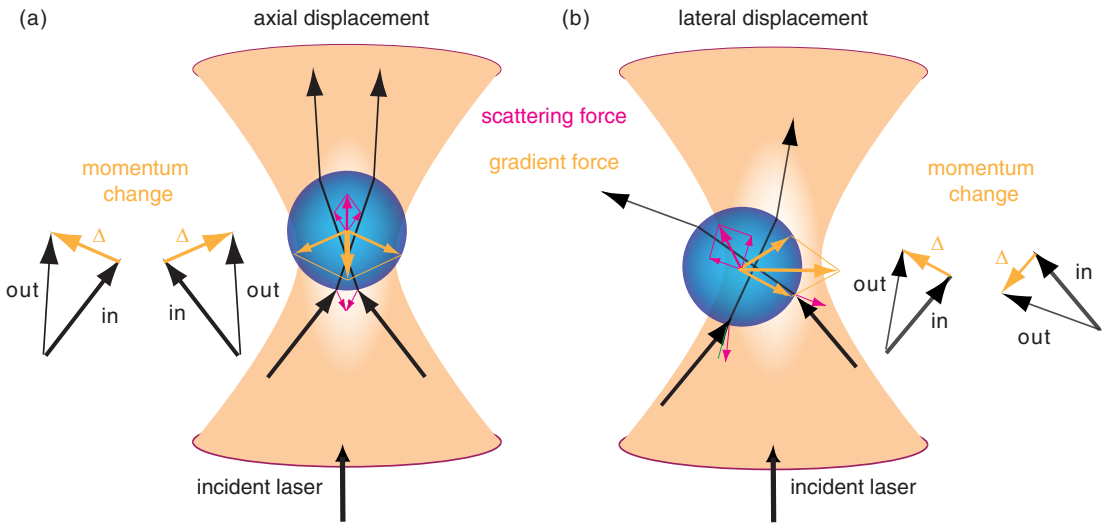

FIGURE 2.1 QUALITATIVE DESCRIPTION OF GRADIENT AND SCATTERING FORCES - The refraction of the two representative rays leads to a net momentum change Δ. the microsphere experience an equal and opposite momentum which generates a restoring force (the gradient force) on the microsphere for both (a) axial and (b) lateral microsphere displacement. On the other hand, the net momentum change caused by reflection leads to a force pushing the microsphere is in the direction of laser propagation (the scattering force). Thickness of the rays indicate their intensity.

scattering force, the thermal fluctuations and the effective weight of the microsphere*.

To calculate the gradient and scattering forces on the trapped microsphere, the momentum transfer from light to the microsphere need to be known. Depending on the microsphere size, there are two approximations where calculations are fairly simple. For microsphere sizes much larger than the trapping waver length ($r \gg \lambda$) ray optics is used, r is the radius of the microsphere and λ is the wavelength of the laser. On the other hand, Rayleigh scattering can be used for sizes much smaller that the trapping wavelength ($r \ll \lambda$). For intermediate sizes comparable to the trapping wavelength, the exact electromagnetic theory is needed.

*There is a number of interactive simulations of optical tweezers available on the web that describe trapping and allow manipulating different parameters for a better understanding. For example: (http://phet.colorado.edu/en/simulation/optical-tweezers) and (http://www.physics.gla.ac.uk/Optics/projects/tweezers/trapsimulation/)

2.1.1 Ray optics

When the trapped microsphere is much larger than the wavelength of the trapping laser, diffraction can be neglected and ray optics is applicable. As described above, forces are due to refraction and reflection caused by the difference in refractive index between the microsphere and the medium. A single ray will be diffracted and deflected a countless number of times. Each time, its intensity, thus its momentum, will change. The change is described by the Fresnel coefficients; the reflectance (R) and the transmittance (T) from which the gradient and scattering forces are calculated [24]:

$$F_{grad} = \frac{n_m P}{c}\left[R\sin 2\theta_i - \frac{T^2[\sin(2\theta_i - 2\theta_r) + R\sin 2\theta_i]}{1 + R^2 + 2R\cos 2\theta_r}\right] \tag{2.1}$$

and

$$F_{scat} = \frac{n_m P}{c}\left[1 + R\cos 2\theta_i - \frac{T^2[\cos(2\theta_i - 2\theta_r) + R\cos 2\theta_i]}{1 + R^2 + 2R\cos 2\theta_r}\right] \tag{2.2}$$

Where P is the laser power in the focus and c is the speed of light in vacuum. As a rule of thump ray optics calculations are valid for sizes $> 10\lambda$.

2.1.2 Rayleigh scattering

If the trapped microsphere is much smaller than the wavelength of the trapping laser then it is safely considered as a point dipole with a dipole moment [25]:

$$\alpha = 4\pi n_m^2 \epsilon_0 r^3 \left(\frac{m^2 - 1}{m^2 + 2}\right)\mathbf{E} \tag{2.3}$$

Where ϵ_0 is the vacuum dielectric constant, m is the relative refractive index ($m = n_p/n_m$) and $\mathbf{E}$ is the electrical field. The gradient force is caused by the Lorentz forces on the dipole and it is proportional to the gradient of laser intensity. Using Eq. 2.3 one can show—based on the energy of a dipole in a field—that the gradient force is :

$$F_{grad} = \frac{2\pi n_m r^3}{c}\left(\frac{m^2 - 1}{m^2 + 2}\right)\nabla I \tag{2.4}$$

Where ∇I is the intensity gradient. The scattering force is due to Rayleigh scattering of the light by the dipole and the net force is in the direction of laser propagation [25]:

$$F_{scat} = \frac{8\pi n_m k^4 r^6}{c}\left(\frac{m^2 - 1}{m^2 + 2}\right) I \tag{2.5}$$

Where $k = 2\pi/\lambda$ is the wavenumber, and I is the laser intensity in the focus. The dipole approximation is valid for microsphere sizes $r \approx \lambda/20$. For larger microspheres, the discrepancy with the exact calculations for the scattering force is significant while the gradient force shows better agreement up to microsphere sizes comparable to the trapping wavelength [25].

2.1.3 Electromagnetic theory

Although ray optics and Rayleigh scattering calculations provide good quantitative estimates in their perspective ranges and an easy-to-understand, qualitative picture of trapping, they are not applicable for microsphere sizes comparable to the trapping laser wavelength. Instead the exact electromagnetic theory is needed to calculate the optical forces on the trapped microsphere.

In electromagnetic theory, trapping is a scattering problem. An incident electromagnetic field on a scatterer creates a field inside the scatterer and a field outside the scatterer. By solving for the three fields plus the scattering cross section of the scatterer, optical forces can be calculated. For a spherical scatter (the trapped microsphere), there is a number of analytical and numerical approaches to solve the problem [26].

An analytical solution of the light scattering of a *plane* wave by a sphere is available via the Mie-Lorenz theory. In Mie-Lorenz theory the electrical and magnetic fields are calculated by solving the Helmholtz wave equation. Next, the incident and scattered waves are expressed as sums of vector spherical wavefunctions (VSWFs) from which the Mie coefficients are calculated. Using the Mie coefficients the microsphere's radiation pressure efficiency—the portion of the total incident momentum that is transfered to the microsphere—is calculated and consequently the trapping force (for an example of the derivation, see Chapter 9 in [27]).

In optical tweezers, the electromagnetic field is not a plane wave but it is a tightly focused beam and instead of the Mie-Lorenz, the generalized Mie-Lorenz theory (GMLT) is used. The GMLT is more complex and computationally demanding. The complexity arose due to the theoretical difficulty to describe the tightly focused beam. There is a considerable work on modeling focused beams, in particular Gaussian beams which are usually used for trapping [28, 29, 30] and on computations of trapping forces using the GMLT [31, 32, 33, 34]. Recently, a comprehensive computational toolbox for optical tweezers

implemented in MATLAB was put forward by Timo Nieminen and colleagues that is numerically robust, stable and fast [35]. The toolbox uses a point matching method for multipole expansion of the strongly focused laser beam [36] and the T-matrix method [37] to calculate the forces and torques on the trapped particle. We used and modified the tool box as described in Chapter 4.

Despite the considerable efforts, agreement between the theoretical calculations and the experimental measurements is rather qualitative than quantitative. The discrepancy is due the aforementioned difficulty of modeling the incident electromagnets field in combination with accounting for distortions on the focused beam such as spherical aberrations. Experimentally, the calibration method affects the accuracy of the measurement. In addition, the methods used for measuring the beam profile in the focus measure intensities and miss the phase information which hinder a fair comparison between theory and experiment.

Chapter 3

Accurate and precise optical tweezers

Here, is a thorough description of our optical tweezers. We describe noise types, its measurements and the methods we used to reduce every type. We describe the different components of the setup and their functions. Finally, we describe how to operate and calibrate the setup. The result of the above is a low-noise setup that is fully automated and capable of measuring accurately sub-nanometer displacements on a time scale of 1 ms–100 s.

3.1 Noise reduction for high resolution measurements

Achieving high resolution measurements using optical tweezers requires a stable, low-noise setup. Noise in optical tweezers stems from (i) the instruments and the environment and (ii) the Brownian motion. Brownian motion is a fundamental limit that can be reduced by averaging the motion over longer periods of time. As for instrumental and environmental noise; clever setup design, better instrumentation, and good isolation from the environment are some of the solutions to reduce it. The following is a short overview of the Brownian motion noise in optical tweezers and how to reduce it followed by a detailed description of how we addressed instrumental and environmental noise in our setup.

3.1.1 Brownian motion

A trapped microsphere is not stationary. It is constantly displaced by the bombardment of the thermally driven molecules of the medium. For a trapped microsphere inertia

plays no role and the microsphere's displacement can be described by its mean square displacement [38, 39]. The mean square displacement of the microsphere along an axis is given by the equipartition theorem [40]:

$$\frac{1}{2}\kappa\langle x^2\rangle = \frac{1}{2}k_B T \tag{3.1}$$

where κ is the trap stiffness, $\langle x^2\rangle$ is the mean square displacement, k_B is the Boltzmann constant and T is the absolute temperature. The root-mean-square (rms) noise caused by the Brownian motion of the microsphere is $\Delta x_{rms} = \sqrt{\langle x^2\rangle}$. Because the Brownian motion is normally distributed with an average of zero, the noise can be reduced by averaging independent measurements. When averaging N measurements the resolution is improved by a factor $1/\sqrt{N}$. Given that the autocorrelation time of the trapped microsphere is $\tau_c = \gamma/\kappa$ where γ is the Stokes drag coefficient, the effective number of samples is $N_e = f_s t_m = t_m/2\tau_c = \kappa t_m/2\gamma$ where f_s is the sampling frequency and t_m is the measurement time. Thus the reduced noise is:

$$\Delta x_{rms} \geq \frac{1}{\sqrt{N_e}}\sqrt{\frac{k_B T}{\kappa}} = \frac{1}{\kappa}\sqrt{\frac{2k_B T\gamma}{t_m}} \tag{3.2}$$

and the rms thermal force noise is:

$$\Delta F_{rms} \geq \kappa\Delta x_{rms} = \sqrt{\frac{2k_B T\gamma}{t_m}} \tag{3.3}$$

with $\gamma = 6\pi\eta r$, where η is the viscosity of the medium and r is the radius of the trapped microsphere. Eq. 3.2 is known as the thermal resolution limit and it can not be beaten. In the literature, a number of equations for the thermal resolution limit exists that differ only by a numerical multiplication factor [23, 39, 40, 41]. We found that the discrepancy stems from the choice of the time limit below which the measurements are considered correlated. In the derivation above we consider the measurements independent after a period of two correlation time constants $2\tau_c$. Aside from the choice of the correlation time limit, the common conclusions are that strengthening the trap or/and measuring for longer times or/and reducing the drag coefficient, all improve the spatial resolution. Interestingly, the trap stiffness has no effect on the force resolution. In addition, the equations show that the improvement of the spatial resolution is on the expense of the temporal resolution since $\Delta x_{rms} \propto \sqrt{1/t_m}$. This explains why, till the moment, the reported sub-nanometer biological measurements are in the 1–5 Hz temporal resolution. For example, *Escherichia coli* RNA polymerase had to be slowed down to 1 base-pair/s

transcription speed in order to measure its 3.4 Å steps [17, 42].

In experiments the microsphere is often tethered to a biomolecule. The stiffness of the tether affects the resolution and Eq. 3.2 is modified accordingly [20, 43]:

$$\Delta x_{rms} \geq \frac{1}{\kappa + \kappa_t}\sqrt{\frac{2k_BT\gamma}{t_m}} \tag{3.4}$$

Where κ_t is the tether stiffness. In case the optical tweezers are operated in a force feedback mode, which is common when measuring step sizes, the trap stiffness drops out, demonstrating that using stiffer tethers is always beneficial for improving the resolution [43].

Finally, resolution can be improved using dual trap optical tweezers instead of single beam optical tweezers (Fig. 2.1). In dual trap optical tweezers two microsphere are trapped with a biomolecule tethered in between. This configuration lowers the Brownian noise despite that the Brownian motion of two microspheres is larger than that of a single microsphere. Due to the tether, the motion of the two microspheres is correlated and the effective drag on the two microspheres is lower than the drag on only one of them. Thus, the two microspheres dissipate thermal energy more efficiently than a single microsphere and as a result the resolution is improved [21, 42]. In summary, when designing a high resolution measurements, experimental parameters should be chosen such that the Brownian motion is reduced.

3.1.2 Environmental noise

Optical tweezers are vulnerable to mechanical and electrical noise coupled in to the setup from different sources. Mechanical noise can be coupled from the surrounding environment in the form of, for example, ground and acoustical vibrations. It can also be coupled in from the different machinery of the optical tweezers like rotating motors. Electrical noise is mainly ground loops induced by potential differences in grounding between connected electronics in the setup. We addressed the different types of environmental noise and used proper measures to reduce them.

Compact design improves the setup stability

The design of the setup can make it less susceptible to environmental noise. Our setup is quite compact ($40\times80\,\mathrm{cm}^2$) which allowed using a small optical top that had a lower width to thickness ratio compared to larger tables usually used in optical tweezers se-

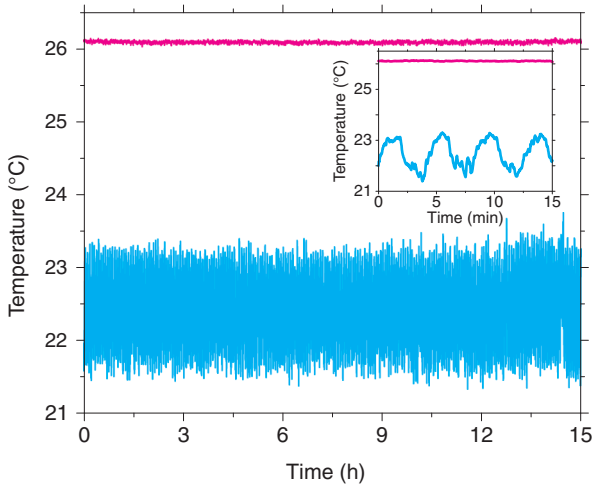

FIGURE 3.1 TEMPERATURE STABILITY IN THE SETUP ROOM - Over a period of 15 hours the temperature in the setup room (—) fluctuated by 60 mK peak-to-peak (0.14 K rms) while the laboratory temperature fluctuated by 2 K (0.53 K rms, —). Inset: temperature fluctuations on a shorter time scale. The effect of the cooling cycle of the air condition is obvious on the laboratory temperature.

tups. The lower width-to-thickness ratio makes the optical top more immune to vibrations [44]. Also, due to the compact size, the laser path is short thus, reducing the effect of air currents and other noise sources on the laser stability. For further stabilization, the laser as well as the optics are kept close the optical top. Additionally, we designed and constructed our own microscope instead of modifying a commercial one. Our microscope is small, rigid and thermally stable.

Dedicated room for isolating the setup from the laboratory

Our first practical step to reduce environmental noise was to construct a small room to separate the setup from the rest of the laboratory. Separating the setup minimized temperature fluctuations and air currents caused by the air conditioning system. As shown in Fig. 3.1, the peak-to-peak temperature fluctuation in the setup room was 33× smaller compared to the rest of the laboratory. Our setup is automated and it is controlled from outside the room limiting access to the setup room only for inserting the sample. Therefore, the equilibrium would be shortly disturbed and quickly restored.

Additionally, we mapped the ground vibrations in the room situated on the third floor using a calibrated accelerometer and found that the vibrations are identical across the room with the strongest vibrations occurring at a frequency around 10 Hz—typical

frequency for upper floor building vibrations [44]. With respect to vibrations, the setup can be built at any location inside the room.

Active damping provides high vibration isolation

Ground and acoustic vibrations coupled to the setup through the optical table lower resolution and need to be damped. Ground vibrations are caused by natural sources like the wind and the grinds of tectonics plates of the earth, and by artificial sources like nearby construction sites, the footsteps of people, vibrations of house machinery like ventilators, pumps, etc. Acoustic vibrations are traveling sound waves through air and walls, and can be caused by fans of the ventilation systems. For damping such noises, optical tweezers setups are built on damping systems that absorb or counteract a disturbance minimizing its effect on the measurements [45, 46].

The standard damping systems used for optical tweezers setups are the passive damping systems [45]. These systems are based on a dash-pot analogy in which disturbances are terminated by a damped air spring [47]. For vibration frequencies above 10 Hz, passive damping systems perform fairly well. On the other hand, due to the resonance frequency of the system of around 1–5 Hz, vibrations with frequencies lower than 10 Hz are amplified instead of being damped. A solution for this problem is to use active vibration damping systems that implement a feedback or feedforward technology . Such systems do not have a resonance and provide better and faster damping than passive systems. Therefore, we choose an active damping system [47, 48].

We used the Vario Basic 60 active damping system (Halcyonics, Göttingen, Germany). To assess the system performance, we measured the power spectral density (PSD) of the vibration velocities of the lab floor, the optical table frame and the optical top of our setup in the vertical and the lateral directions. An example of the measurement is shown in Fig. 3.2 for the vertical direction where vibrations are strongest. As expected the vibrations of the ground and the frame were identical except for additional noise at the frame resonances frequencies (150–400 Hz). On the other hand, the vibrations on the optical top where lower than the ground due to the damping system. For example, the ground vibrations at 10 Hz were damped to −33 dB (transmissibility = 0.002) on the optical top.

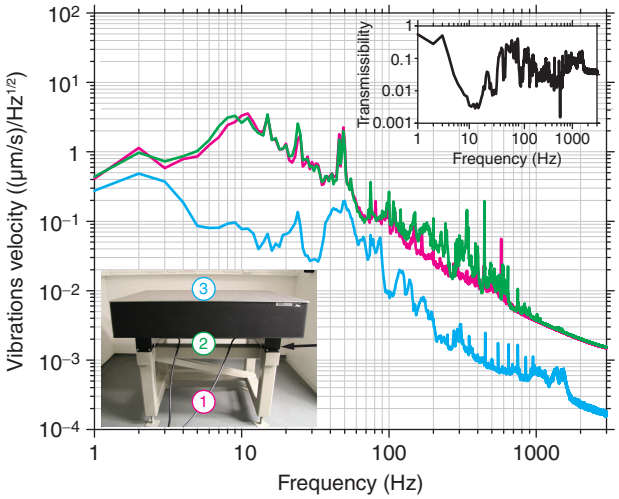

FIGURE 3.2 ACTIVE VIBRATION DAMPING - Using a calibrated accelerometer we measured the power spectral density of the vertical vibrations velocity of (1) the ground (—), (2) the optical table frame (—) and (3) the optical top with active vibration damping (—). Inset upper: the transmissibility (T_r = optical top motion/ ground motion) of the damping system for the vertical vibrations. Inset lower: an image of the optical table. The arrow points to one of the two active damping elements. The numbers correspond to the vibration measurement positions.

Furthermore, we measured the vibrations of two other optical tweezers setups for comparison with our setup: the first setup used an air pressure passive damping system located in similar environmental conditions, and the second is built on a passively damped concrete block located in a basement. The comparison between the three setups (Fig. 3.3) shows the advantage of the active over passive damping over the whole bandwidth especially in the ≤10 Hz range. In addition, our system performance was comparable to the damped concrete block which is highly vibration resistant due to its large mass, low vibration environment and a supporting damping system.

We also considered one additional factor to improve damping; the choice of the optical top. The dimensions and structure of the optical top influence the damping. Shorter and thicker optical tops shift the resonance to higher frequencies making the setup less vulnerable to the high-amplitude, low-frequency disturbances. We used a $80 \times 100\,\mathrm{cm}^2 \times 20\,\mathrm{cm}$ honeycomb optical top (1HT08-10-20, Standa, Lithuania). Honeycomb tops are known for their high rigidity and fast thermal equilibrium plus a practical weight in comparison to other types such as granite optical tops [44, 46]. Finally, once finished

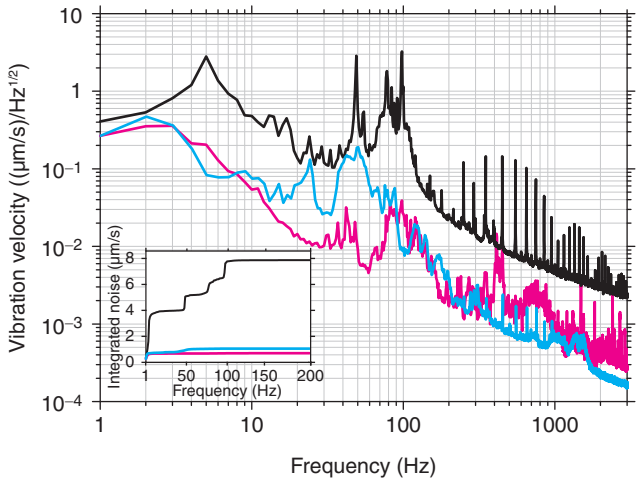

FIGURE 3.3 ADVANTAGE OF ACTIVE VIBRATION DAMPING - Power spectral density measurements of vertical vibration velocities of (1) our active damping system (—), (2) a passive damping system (—) and (3) damped concrete block placed in a basement (—). The sharp peaks at multiples of 50 Hz are electrical noise and are not real vibrations. Inset: integrated noise for the three systems. Up to 10 Hz the active damping system performed equally to the damped concrete block. At higher frequencies, the active system had more noise caused by higher noise amplitudes in the 10–100 Hz which is observed as a step in the integrated noise curve. Beyond 100 Hz the active system performed better than the damped concrete block. On the other hand, the passive system had much higher noise than the active system, 5× at 10 Hz up to 8× at 200 Hz.

the setup was enclosed in an acoustically isolating box that provided not only acoustic isolation but also reduced air currents.

Thermal drift

Thermal drift is another mechanical noise caused by the temperature gradients within the setup. It is characterized by its low frequency leading to a drift on the order of 1-2 μm/min. We deal with this type of noise in Chapter 5.

Ground loops

The dominant type of electrical noise in optical tweezers is ground loops. Ground loops are voltage fluctuations on the measurement signal usually observed at the voltage source frequency or its harmonics. Ground loops are induced if two or more interconnected electrical devices (e.g. an acquisition card and a controller card) have a potential difference between their grounds. The potential difference induce a flowing current loop between the connected devices, hence, the name. Since there is a minute, yet, existing

resistance on the connecting wires an AC noise voltage is induced and it is detected as part of the measurement signal. Moreover, ground loops behave as an antenna that can pick up electromagnetic interference (EMI) noise from nearby sources such as power lines and power supplies [49].

To reduce electrical noise in our setup we made the following:

- Established a central grounding point to which all devices are connected. The grounding point is directly connected to the building central ground via a 16 mm^2 cross-section cable.
- Electromagnetic induction sources such as power supplies are kept at a distance from other devices since the induced signal is inversely proportional to the distance from the source.
- We added the devices sequentially and measured the noise after each addition. Also, we measured the noise for different device combinations to investigate the noise contribution of each device.
- We used shielded cables and grounded the shields as well.

3.1.3 Instrumental noise

Besides environmental noise, additional noise is caused by the components of the setup. For example, power and pointing instabilities of the trapping laser (see next section), laser misalignment due to imperfections in the used optics and electrical noise of the devices used. Instrumental noise is reduced by using adequate and up-to-date equipment and by careful alignment. For example, we used IR optimized lenses for the trapping laser. The same goes for our detection system as well. Our data acquisition and control devices are stable with very low noise.

During an experiment we monitor the signal from two active components: the piezo stage and the steering piezo tilt mirror that are involved in the calibration and the force feedback. We measured the noise of both and it was in the sub-ångstrom range (Fig. 3.4a).

3.1.4 Low noise and sub-nanometer resolution

To assess the efficiency of our noise reduction measures, we measured and analyzed the noise by PSD (frequency domain) and Allan deviation (time domain) analysis [40, 41].

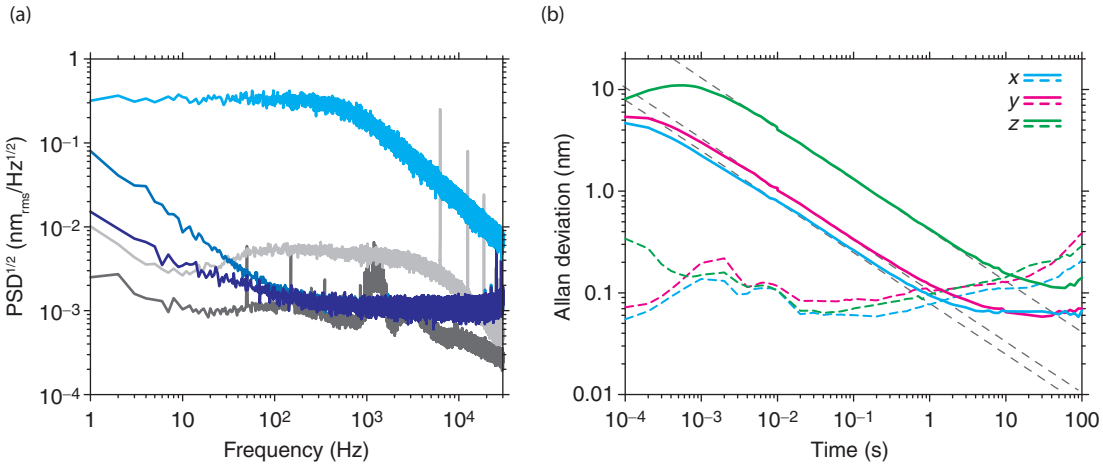

FIGURE 3.4 NOISE AND RESOLUTION - (a) Noise spectra of the steering piezo mirror (—), the piezo stage (—), the dark signal of the detector (—) and the trapping laser (—). For comparison, the spectra of trapped 0.528 μm microsphere (—) is measured. The sharp peaks on the piezo stage are due to electronic noise on the controller. Also, the peaks on the steering mirror stage at 50 and 150 Hz are electrical noise and does not reflect real movement. Due to the mirror stage resonance, additional peak was observed around 1000 Hz. (b) Allan deviation of a trapped 0.528 μm microsphere (solid lines) and a fixed microsphere of the same size (dashed colored lines). The dark dashed lines are the thermal limits for the three axes calculated using Eq. 3.2 with the experimental parameters κ_x = 0.106 pN/nm, κ_y = 0.85 pN/nm, κ_z = 0.034 pN/nm, T = 298 K and r = 0.264 μm. The measurement was done over a period of 1000 seconds.

Power spectral density analysis gives information about the type of the noise and its frequency and amplitude. Electrical noise from power lines appears as sharp peaks at the frequency of 50 Hz or its harmonics while mechanical noise peaks are broad with no frequency preference. We measured the dark signal of our detector which forms the base line of the electrical noise. Also, we measured a "bright" laser signal where there is no microsphere trapped which reflects the noise on the trapping laser. Finally, we measured the signal from a trapped microsphere and compared it to the previous two (Fig. 3.4a). The PSD of the dark and bright signals showed sub-ågestrom noise levels reflecting the high stability of the setup. The measurement signals were well above the noise levels

Besides the PSD, we calculated the Allan deviation to measure the noise at different time periods especially for periods > 1 s where low frequency noise like drift is dominant. The Allan deviation is given by [40, 41]:

$$\sigma_x(\tau) = \sqrt{\frac{1}{2}\langle (x_{n+1} - x_n)^2 \rangle_\tau} \tag{3.5}$$

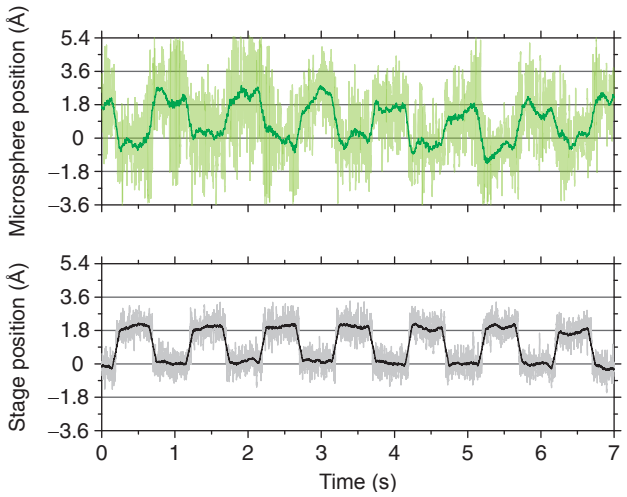

FIGURE 3.5 SUB-BASEPAIR STEPS - With a fixed microsphere on the surface of a flow cell, the piezo stage was oscillated laterally with a square signal at 1.8 Å amplitude and the microsphere position was measured. Data were acquired with a sampling frequency of 10 kHz and are displayed with 10 Hz (200 Hz, shaded colors) bandwidth obtained by adjacent averaging.

where x_n is the average of the microsphere position over the sample n and τ is the time per sample. We measured the Allan deviation for a trapped microsphere and compared it with the thermal limit given by Eq. 3.2. We also made the same measurement for a microsphere fixed to the flow cell surface. A fixed microsphere has is hardly susceptible to Brownian motion and its Allan deviation is a measure of the environmental and instrumental noise of the setup (Fig. 3.4b). For the trapped microsphere, for all axes, the Allan deviation reaches a maximum at $\tau = \pi\tau_c$ and decays with a slope of $-\frac{1}{2}$ for $\tau > 2\pi^2\tau_c$ [41]. Compared to the thermal limit, the Allan deviation is lower at short measurement times due to correlation in the measurements. For longer measurement times the Allan deviation adhered to the thermal limit closely before deviating again around $\tau \geq 1$ s due to low frequency noise. On the other hand, for the fixed microsphere the Allan deviation maintained a sub-nanometer noise level that was rather constant up to 1 s where low frequency noise came into effect. Beyond 1 s the fixed microsphere had higher noise than the trapped one since the trapped microsphere is less sensitive to low frequency noise such as drift. The trapped microsphere moves relative to the trap center unaware of the trap or laser movement relative to the sample unlike the fixed microsphere that is progressively separated from the drifting optical trap.

The results of the above analysis demonstrates the high stability of the setup and its capability to resolve sub-nanometer displacements on a time scale starting from 1 ms laterally and 10 ms axially up to 100 seconds and possibly longer for a moderately stiff trap. For example, according to the Allan deviation, it should be possible to resolve base pair steps of 3.4 Å at a 1 base pair/s rate. Indeed, we were able to measure sub-base pair steps. We oscillated the piezo stage with a square wave at 1 Hz frequency and 1.8 Å amplitude and monitored the position of a fixed microsphere on the surface of a flow cell. As shown in Fig. 3.5 it was possible to measure the 1.8 Å microsphere movements. Axially, the setup was able to resolve 2.7 Å steps produced in the same fashion.

It should be mentioned that, under normal working conditions, the resolution is degraded by the drift in the setup. Closing the shutter for only 5 s caused a 20 nm drift and the setup required 200 s to equilibrate and restore its resolution. To reduce drift and maintain the resolution capabilities of the setup we implemented a temperature feedback on the objectives to restore the thermal equilibrium fast and to stabilize the objectives temperature at a millikelvin precision as discussed in more details in Chapter 5.

3.2 Construction of the optical tweezers

Here we present the optical tweezers. The design and photos of the setup are shown in Fig. 3.6 and Fig. 3.9. We follow the path of the trapping laser from the laser head up to the detection on the microscope describing the different components of the setup and their functions. Protocols for constructing the setup and relevant control measurements can be found on the Appendix.

3.2.1 Stable IR laser for biological studies

When using optical tweezers for high resolution biological studies, the trapping laser needs to meet a number of requirements as discussed below:

Wavelength

When choosing the trapping laser wavelength for biological samples, optical damage is the main concern [9]. Due to the high laser intensity at the center of the trap, the sample is prone to optical damage caused by localized heating, 2-photon absorption or toxic oxygen radicals. Studies had shown that laser wavelengths in the near-IR are the least damaging to biological matter, in particular the wavelengths 830, 970 and 1064 nm

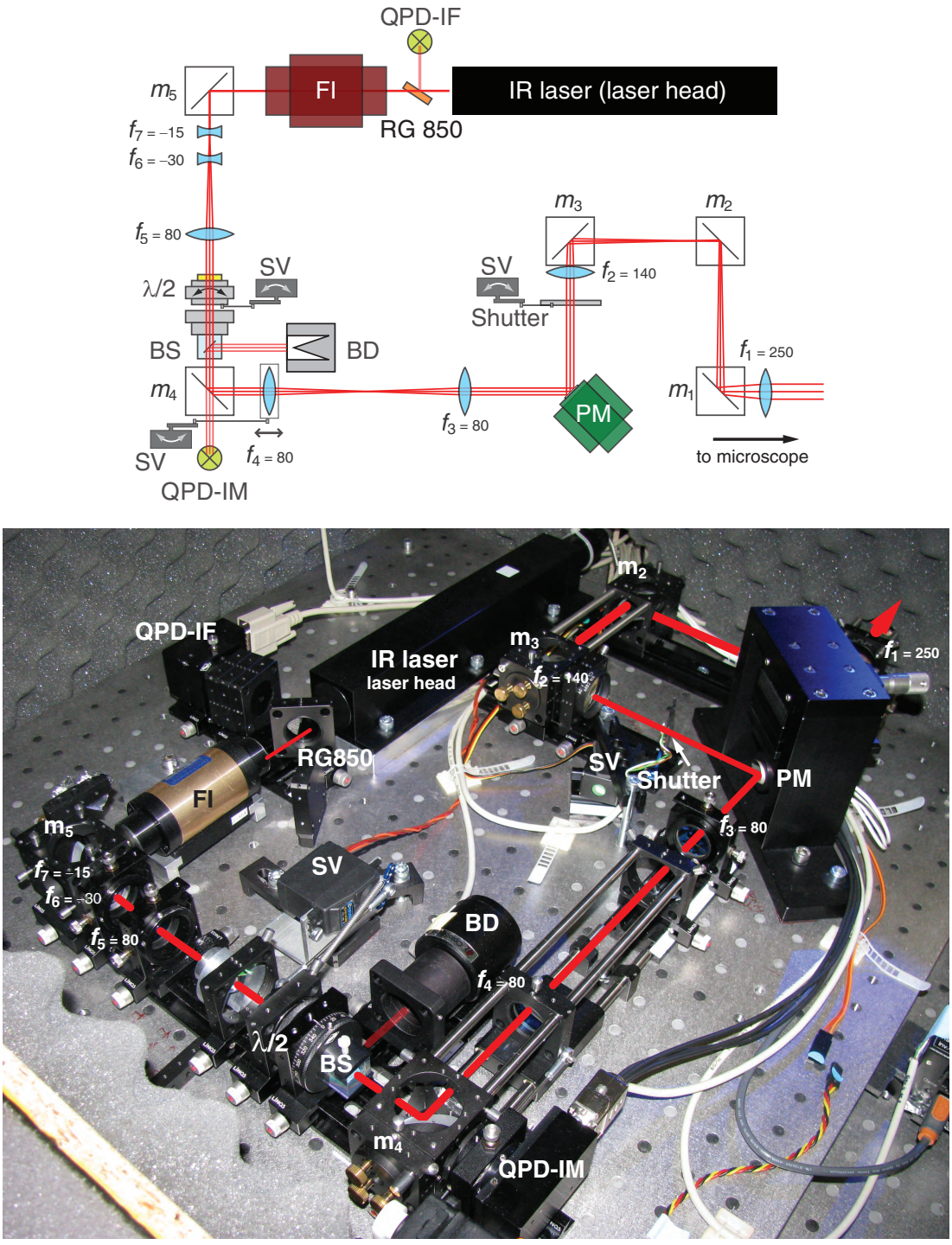

FIGURE 3.6 OUR OPTICAL TWEEZERS - Schematic drawing and a photo (March 2011) of our optical tweezers setup showing the laser path up to the microscope. The labeled components are: infra red laser (IR laser), quadrant photodiode for laser intensity feedback (QPD-IF), RG850 filter (RG850), Faraday isolator (FI), laser mirror (m_{1-5}), lens (f_{1-7}), half wave plate ($\lambda/2$), polarizing beam splitter (BS), servo (SV), beam dump (BD), quadrant photodiode for intensity monitoring (QPD-IM), piezo mirror stage (PM). All focal lengths are in mm. The red line is a guide to the eye for the laser path.

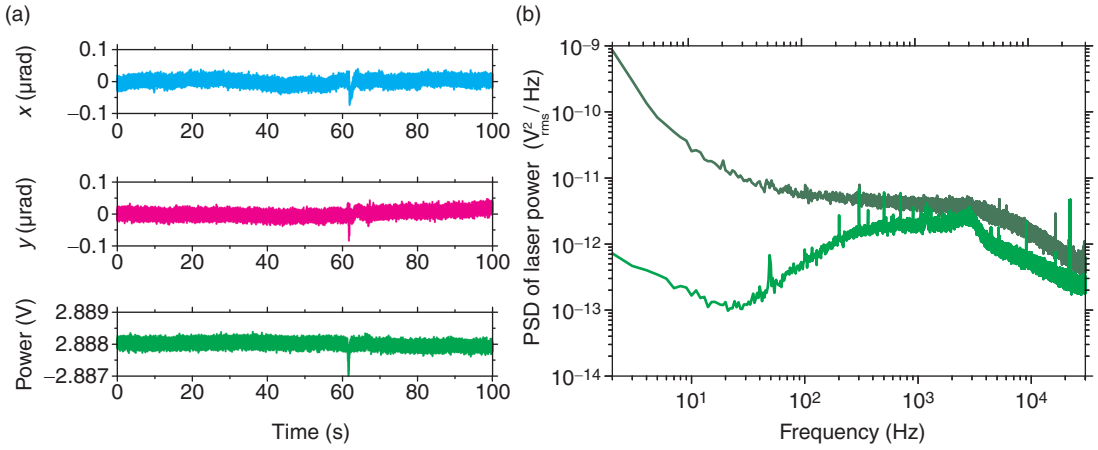

FIGURE 3.7 LASER POINTING AND POWER STABILITY - (a) For the 2 W laser, over a period of 100 seconds the laser spot on a QPD fluctuated about its average position by 0.01 μrad in the x and y directions. In our setup, such fluctuation caused a 0.1 Å trap displacement in the sample plane. The sum signal (i.e. the laser power) on the QPD had a COV of 3×10^{-5} with the laser feedback on. Signals were measured with 1 kHz sampling rate at 50 cm from the laser head. (b) A PSD of the laser power with the laser feedback off (—) and on (—).

[50, 51, 52, 53]. Of the three wavelengths, the 1064 nm wavelength is the most common in optical tweezers due to its availability in high powers, high pointing and power stability and reasonable prices [45, 54].

Pointing and power stability

An important requirement in the trapping laser is to have high pointing and power stability. Pointing fluctuations lead to lateral movements of the trap in the sample and power fluctuations change the trap stiffness. If external sources of fluctuations like vibrations or air currents are damped, then the stability of the laser depends mainly on its type and technology [55]. Diode pumped solid state (DPSS) lasers have proven to be highly stable compared to other types such as diode lasers. In our setup, we first used a 2 W diode pumped neodymium yttrium aluminium garnet (Nd:YAG) diode pumped laser which was later replaced by a 5 W diode-pumped neodymium yttrium vanadate ($Nd:YVO_4$) laser, both lasing at 1064 nm (Smart Laser Systems, Berlin, Germany). Both lasers were linearly polarized and had a Gaussian beam profile with a beam quality factors ($\mathbf{M}^2$) = 1.12 and 1.08 for the 2 W and 5 W respectively. We measured the pointing and power stability by monitoring the laser using a QPD placed at 50 cm from the laser head (see Appendix). Over 1000 seconds, the laser pointing stability was 0.02 μrad (measured as standard deviation) in the x and y directions. Such fluctuation caused less than

0.2 Å movement in the sample plane. For 100 seconds the stability was a factor of two better. As for power stability, the laser power had a coefficient of variation (COV, standard deviation divided by the mean) of 3×10^{-4} and 5×10^{-4} over 1000 seconds measured at a sampling rate of 1 kHz for the 2 and 5 W lasers respectively. To further stabilize the laser power, we used a feedback circuit that improved the stability one order of magnitude (Fig. 3.7).

Faraday Isolator

Due to the setup optics, a part of the laser is reflected back into the laser head and destabilizes it. To protect the laser from back reflections we used a Faraday isolator (OFR-IO-3-1064-VHP, OFR, Munich, Germany) placed after the laser head. The Faraday isolator allowed the light to pass in one direction while blocking it in the reverse direction. After the isolator, the laser was expanded by a 3-lens Galilean telescope.

3.2.2 A 3-lens Galilean telescope for smooth laser expansion

To be able to stably trap microspheres, the laser beam entering the exit pupil of the objective should exceed a minimum width at the back focal plane of the trapping objective. We expanded the laser in two stages; (i) using a three lens Galilean telescope and (ii) using a Kepler telescope. Using the Galilean telescope the laser is expanded by 3.5× to 2.9 mm diameter beam. The 3-lens Galilean telescope had two advantages. First, the telescope had no internal focus. Focusing a high power laser changes the refractive index of the surrounding atmosphere causing pointing instabilities. Second, it was possible to change the magnification in a smooth continuous fashion by moving two lenses (f_5 and f_6) along the optical axis without the need to replace any of the lenses. We did not expand the laser more than 7× by a single telescope; otherwise the laser would suffer from spherical aberrations.

3.2.3 Automated laser intensity control in the sample

In optical tweezers, controlling the trap stiffness is done by changing the laser intensity in the focus. It is possible to change the laser intensity by changing the pumping diode current, but this is not practical as the laser needs 10–15 minutes after each change to retain its stability. A practical and simple solution is a combination of a rotatable half-wave plate ($\lambda/2$) (Zero order 02WRC027/1064, Melles Griot, Bensheim, Germany)

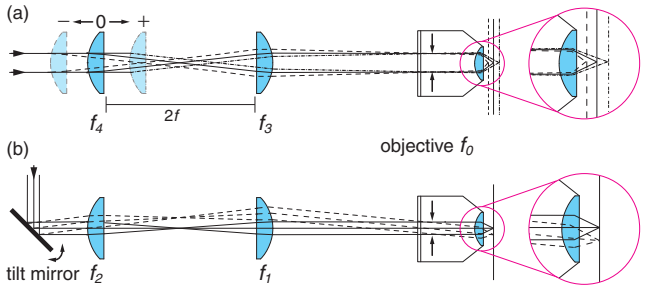

FIGURE 3.8 DYNAMIC 3D CONTROL OF THE TRAP - Schematic drawing of 3D control of the trap in the sample. (a) Axial direction. Moving f_4 in the + direction cause the laser beam to diverge at the back focal plane of the trapping objective. The objective focuses the divergent beam beyond its focal plane. Moving f_4 in the − direction leads to the exact opposite. (b) Lateral direction. A mirror is placed in a conjugate plane to the back focal plane of the trapping objective. Tilting the mirror changes the angle at which the laser beam enters the back focal plane. Depending on the angle, the laser is moved laterally. The arrows inside the objective show the size of the beams at the back focal plane of the objective.

followed by a polarizing beam splitter (Linos, Germany). Rotating the wave plate rotates the laser polarization relative to the beam splitter transmission axis. The amount of laser passing through the beam splitter depends on the angle between the laser polarization and the transmission axis. We used a calibrated PC-controlled servo for rotating the wave plate and monitored the intensity using a QPD (QPD-IM). The reflected laser light form the beam splitter was directed into a beam dump where it was absorbed and dissipated to heat.

3.2.4 Dynamic 3D control of the trap in the sample

To be able to control the optical trap dynamically in 3D within the sample, we used two control units for (i) the axial and (ii) the lateral directions. Axial position of the trap can be changed by making the trapping laser beam diverge or converge at the back focal plane of the objective (Fig. 3.8a, [56]). In practice, we used a 1:1-telescope that has a movable lens ,f_4, that can be translated along the optical axis using a PC-controlled servo. The focal plane of the fixed lens, f_3, was kept at a conjugate plane with the objective back focal plane. Reducing (increasing) the distance between the lenses by translating the movable lens caused the laser to diverge (converge) at the back focal plane of the objective while maintaining its size. Maintaining the beam size at the back focal plane insures that the filling ratio (beam width divided by the exit pupil width, chapter 4) is not changed. The axial range Δz in the sample is related to the movable

lens travel range $\Delta_{movable}$ by [56]:

$$\Delta z = \left(\frac{f_0 f_2}{f_1 f_3}\right)^2 \Delta_{movable} \tag{3.6}$$

where $f_0 = 2\,\text{mm}$ is the focal length of the trapping objective. In our setup the movable lens had a traveling range of 53 mm corresponding to a measured Δz of 4.8 μm in the sample compared to 10 μm from eq. 3.6. So far we did not find the reason for this discrepancy. Besides moving the trap axially, the unit can be used to reduce spherical aberrations caused by the refractive index mismatch between the immersion oil and the sample medium for high NA objectives [57]. Also, it can be used to match the trapping focal plane with the imaging plane that differ due to chromatic aberrations.

To move the trap laterally in the sample plane, we used a piezo tilt mirror (Nano-MTA2/2X, MadCity Labs, Madison, USA) positioned in a conjugate plane to the objective back focal plane. When the mirror is tilted, the beam pivots around the back focal plane center. Consequently, the focus is displaced laterally in the specimen plane . The lateral displacement Δr in the sample plane is related to the angular tilt of the mirror $\Delta\theta$ by (Fig. 3.8b,[56]):

$$\Delta r = 2\frac{f_0 f_2}{f_1}\Delta\theta \tag{3.7}$$

The measured range was 10.1 μm in a good agreement with the calculated 11.7 μm (for angular range of 5 mrad) knowing that a technical problem in the mirror prevented us from utilizing the whole angular range.

After the piezo mirror, the laser in expanded once more by a Kepler telescope (f_2 and f_1) built on a U-shaped optical path. Beside expanding the laser beam, the telescope images the tilt mirror onto the exit pupil of the trapping objective. The telescope expanded the laser by 1.78× to a final beam width of 5.1 mm. The advantage of having a U-shaped optical path is the ability to adjust the distance between the telescope lenses by moving the mirrors m_2 and m_3 simultaneously; a handy option than can be used when one of the telescope lenses is exchanged or when additional optics are added. After the expansion, the laser beam was reflected into the microscope using a dichroic mirror.

3.2.5 The microscope

We designed and constructed a home-built microscope (Fig. 3.9). The microscope is made of anodized aluminum chosen for its high stiffness and good thermal properties that

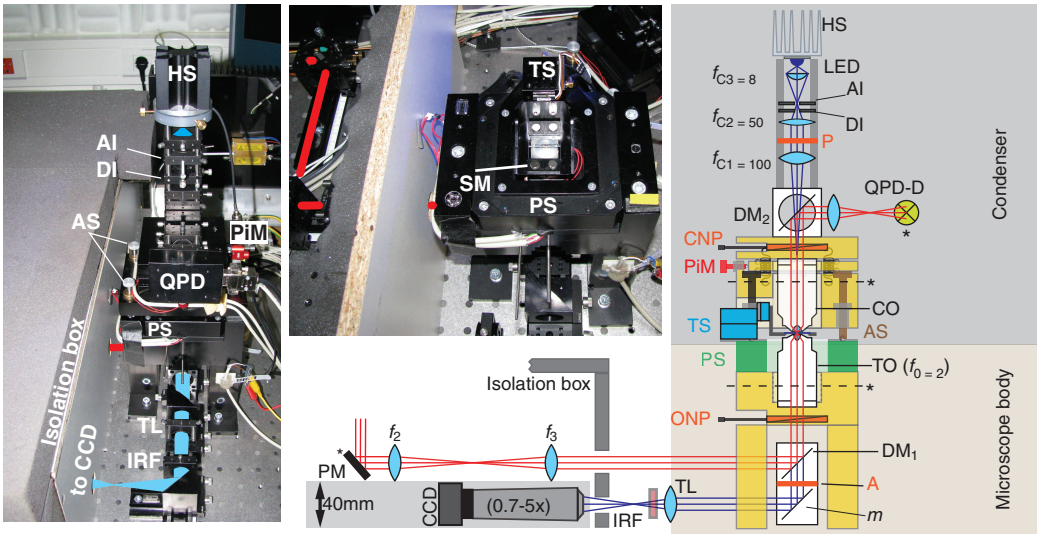

FIGURE 3.9 THE MICROSCOPE - Schematic drawing and photos of the microscope (March 2011). The components are: heat sink (HS), light emitting diode (LED), Lens (f_{c1-3}), Aperture iris (AI), Field diaphragm iris (DI), polarizer (P), condenser Nomarski prism (CNP), quadrant photo diode for detection (QPD-D), dichroic mirror (DM_{1-2}), condenser objective (CO), pico motor (PiM), traveling stage (TS), adjustment screw (AS), piezo stage (PS), trapping objective (TO), objective Nomarski prism (ONP), analyzer (A), mirror (m), tube lens (TL), infrared blocking filter (IRF), charge-coupled device (CCD), super magnets (SM, middle photo). The dashed lines across the trapping and condenser objectives indicate the back focal plane. The asterisks indicate conjugate planes. All focal lengths are in mm. The shaded areas outline the two main parts of the microscope: the microscope body and the condenser. In the schematic, the laser is presented by red lines and the imaging visible light by blue lines. In photos, red and cyan lines are guides to the eye for the trapping laser and the LED illumination light, respectively.

makes the microscope mechanically and thermally stable. The microscope is practical to use, easy to modify, and cost efficient and consists of two main parts: the microscope body and the condenser. The microscope body forms the base of the microscope. It stands on three thick legs attached to the optical top. The trapping objective (infinity corrected CFI S Fluor 100×/0.7–1.3 oil objectives, Nikon, Japan) is screwed into the microscope body for more stability and it is thermally stabilized by a temperature feedback (see Chapter 5). The sample ($22 \times 22\,\mathrm{mm}^2$) is fixed on the sample holder by powerful magnets (Supermagnete, Uster, Switzerland). Positioning the sample relative the objective is made by two stages: (i) a long-range travel piezo-inertial stage ($8 \times 8 \times 3.5\,\mathrm{mm}$ in x, y, and z respectively, MS30(15), Mechonics Ag, Munich, Germany) used for exploring the sample and (ii) a nanopositioning stage ($30 \times 30 \times 10\,\mu\mathrm{m}$ in x, y, and z respectively, P-733.3DD, Physik Instrumente, Karlsruhe, Germany) with sub ångstrom resolution used for accu-

rate displacements and calibration of the trap.

The condenser stands on top of the microscope body on three fine adjustment screws (9S127N-25, Standa, Lithuania). The height is set such that the trapping objective and an identical condenser objective are confocal with respect to the trapping laser. The condenser objective is aligned relative the trapping objective using two PC-controlled pico motors (Tiny Pico-motors 8353, New Focus, San Jose, USA). For illumination and detection, the condenser is equipped with a 4-rod microbench system (Linos, Germany) to easily insert, replace and position the needed components.

Trapping and detection

After being reflected by the dichroic mirror DM_1, the laser is focused into a diffraction limited spot hereby forming the optical trap in the sample. In order to prevent shearing of the laser by the Nomarski prisms used for DIC imaging, the laser polarization is made parallel to the shear axis of the prism. Next, the laser is collected by the condenser objective and since the condenser objective is confocal with the trapping objective the laser emerges collimated. Afterwards, the laser is reflected out of the imaging path by a dichroic mirror to a lens that forms an image of the back focal plane of the condenser onto a QPD for position detection.

For detecting the position of the microsphere in 3D, we used a non-imaging interferometry based detection. Interferometric detection provides high spatial and temporal resolution on the sub-ångestrom and microsecond levels limited by noise on the detector and the setup [45, 58, 59]. We used the so called back-focal-plane detection in which the far field interference of the scattered laser light from the trapped microsphere with the unscattered laser light is monitored in the back focal plane of the condenser objective [19, 43]. Displacement of the trapped microsphere within the focus leads to changes in the laser interference pattern in the back focal plane which are recorded as difference and intensity changes on the QPD. For small displacements from the focus center ($\approx \pm 200\,\text{nm}$ depending on the microsphere size) the signals from the QPD are proportional to the displacement.

Back-focal-plane detection is intrinsically more sensitive to lateral placements than axial ones because the lateral signal scales with the ratio of the displacement to beam waist at he focus while the axial signal scales with the displacement to the Rayleigh range which is 2–3 times larger than the beam waist [19]. In addition, axial detection

by the QPD is also less sensitive than the lateral one. The lateral detection is a differential measurement while the axial one is a minute change of the intensity over a large background signal. To improve the axial detection, we reduced the NA of the condenser objective. Axial displacements of the trapped microsphere lead to intensity changes in the center of the interference pattern. On the other hand, the signal on the edges of the interference pattern merely increase the background and thus degrades the detection signal [60]. By reducing the NA of the condenser the edges are blocked and the axial sensitivity is improved. On the other hand, we found that reducing the condenser objective NA degraded the lateral sensitivity. We measured the axial and the lateral sensitivities as a function of the condenser objective NA and found that an NA of 1.1–1.2 was a good compromise. Possible solutions to improve axial detector sensitivity is to detect the back reflected laser light instead of the forward transmitted light [61, 62] or to split the light for lateral and axial detection. Back reflected light is much weaker in intensity but there is no large background such that the axial changes are more pronounced. In principle, back reflection is possible on our setup but we did not implemented since forward detection was sufficient for our experiments.

Detection QPD: For detection, first we used a standard silicon QPD (QP50-6SD2, Pacific Silicon Sensor, Westlake Village, USA). Due to its partial transparency in the IR region, the QPD acted as a low pass filter with a cut off frequency around 8 kHz which is problematic when stiff traps are used [63]. We replaced the QPD with a position sensitive detector (DL100-7PCBA3, same company) which had a high cut off frequency around 20 kHz. Finally, we use a IR-optimized silicon based QPD that had a cut off frequency of 150 kHz operated in a reverse bias mode (QP154-Q-HVSD, same company).

Imaging the sample

Imaging the sample is possible with bright field microscopy and differential interference contrast (DIC). We used an ultra bright LED (Luxeon Rebel "royal blue" 447.5 nm, LED-Tech, Germany) for illumination. Using an LED as a light source is sufficient to image single microtubules with video-enhanced differential interference contrast (LED-DIC [64]). The sample is uniformly illuminated according to Köhler illumination to utilize the full potential of the objectives. The sample is imaged by the trapping objective and the image in projected onto a CCD camera (Lm130m, Lumenera, Canada). Changing the magnification of the image is possible using an optical zoom (0.7–4.9× zoom, Sill optics, Wendelstein, Germany). we used an infrared blocking filter to block laser light (mainly reflected from the sample) from reaching the camera.

In our setup we used DIC as our default imaging method rather than bright field microscopy. Switching to DIC from bright field is done by adding two Nomarski-DIC prisms and two polarizer. The polarizers are set in a crossed polarization configuration with their transmission axis at 45° to the shear axis of the DIC prisms. Although straight forward, we had the difficulty that DIC imaging was not possible with our objectives and the current model of DIC prisms offered by the manufacturer. To have DIC imaging, we had the choice of either changing the condenser objective or using older models of DIC prisms on the expense of lower image contrast. We chose the later[1]. Improving the contrast was possible by reducing the NA of the illumination [65]. To avoid interfering with the laser detection, we made the illumination NA independent of the condenser objective by placing an iris between the LED and the condenser in a conjugate plane to the back focal plane of the condenser.

3.2.6 Temperature

We implemented a total of 12 temperature sensors (Pt100, RS, Germany) for measuring the temperature of different parts of the setup. We measure the temperature of the trapping objective, the condenser objective and the microscope. Also we measure the temperature of the components that can lead to temperature gradients: the laser head, the CCD camera, the laser dump and the shutter. In addition we measure the temperature of the pumping laser heat sink, inside the isolation box, inside the setup room and outside the setup room. We also added a hygrometer for measuring the humidity in the setup room.

3.3 Control and data acquisition

Controlling the setup is automated via a custom-written software programmed in LabVIEW (National Instruments, Austin, USA). The pico motors used for aligning the condenser objective and the long range piezo stages used to explore the sample and to position the detection QPD can be moved in steps or in a continuous fashion at different speeds. The LED illumination can be also smoothly changed. The intensity, movable lens and shutter are controlled via servos. Each servo moves in response to a short electrical pulse during which a high current is applied to the servo. It could happen that the current is sustained after the electrical pulse ends, or, in some cases, when the servo is unable to complete its movement due to internal or external reasons. To protect

[1] It was a strike of luck that we got two out of five total remaining prisms world wide!

the servos against sustained high currents, we programmed a protection routine that monitor the servos currents and issues a timed sound alarm in case of a sustained high current before shutting down the power supply if no action is taken by the user. For imaging, we used a routine that is able of controlling the CCD operation parameters, image processing, tracking selected objects, measuring intensities, and controlling the piezo stage position. The piezo stage and the piezo tilt mirror are controlled using a 16-bit high speed output card (NI 6733, National Instruments, Munich, Germany). The bit resolution (smallest output signal) for the piezo stage was 0.9 nm[1] and for the mirror it was 0.15 nm relative to the sample plane. A routine reads the measured temperature of all sensors plus the humidity in the setup room and saves the measurements on a daily bases. To stabilize the temperature of the trapping and condenser objectives we programmed a proportional-integral-derivative (PID) feedback. The feedback stabilized the temperature with milli-Kelvin precession by regulating the voltage of three heaters installed on the objectives updated every 0.25 s. To prevent overheating the objectives, the feedback is only operational in a predefined temperature range.

During a measurement we acquire eight signals using a 24-bit acquisition card that has a 50 kHz alias free bandwidth (NI 4472B, National Instruments, Munich, Germany). The signals are the three spatial axes from the detection QPD, the three monitor signals from the piezo stage axes and the two monitor signals from piezo tilt mirror. For calibration, we use a routine for measuring, averaging and fitting the power spectral density of the data as a function of distance from the flow cell surface. For measurements, the data are read using one of many routines programmed to meet the requirements of different experiments. The setup can be operated in a "standard" mode or in a force feedback mode. In the force feedback mode, the setup maintains a constant force load on the target molecule and is used to measure the time dependent motion of the molecule [43].

3.4 Calibration

With the absence of accurate theoretical calculations, empirical calibration of the optical tweezers is needed for quantitative force and displacement measurements. Since a force exerted or sensed by the trapped microsphere is $F = \kappa \Delta x$, both the trap stiffness κ and he displacement from the trap center Δx need to be known. Displacements are measured by position detectors whose output signals are not in meter. Thus, a detector

[1] To obtain the 1.8 Å steps for testing the resolution capabilities of the setup, we had to use a potential divider to make the bit resolution smaller.

output-to-meter conversion factor is needed—also known as the displacement sensitivity β. Calibrating the optical tweezers means to accurately measure the trap stiffness and the displacement sensitivity.

3.4.1 Position detection calibration

The position of the trapped microsphere can be detected by imaging methods or by non-imaging interferometric methods. Among imaging methods, the simplest and the most common is to use a camera which is usually included in the setup. It is possible to measure the absolute position of the microsphere with a sub-pixel resolution using centroid-finding algorithms. Standard cameras have low temporal resolution due to its low frame rates, $\approx 25 - 120$ Hz [45]. To improve the temporal resolution, high-speed CCD cameras and complementary metal oxide semiconductor (CMOS) cameras have been used. Such cameras offer frame rates of a few kHz limited by the computer's CPU power and the capacity of the volatile memory. Nowadays, imaging with frame rates up to 5 kHz and sub-nanometer resolution is possible [66, 67, 68]. Cameras are calibrated by using a micro-ruler or by displacing a fixed microsphere a known distance using a piezo stage to get the pixel-to-meter conversion factor.

The most common interferometric detection—and among all detection methods in optical tweezers for that matter—is the back-focal-plane detection which is already covered in Sec. 3.2.5. In back-focal-plane detection the output signal of the QPD is in volts and it can be calibrated by scanning a fixed microsphere through the laser focus by known distance [19]. It is also possible to calibrate the detector by power spectral analysis (see below).

3.4.2 Trap stiffness calibration

There is a number of calibration methods for measuring the trap stiffness [45, 69]. A simple method in based on statistical analysis of the thermal fluctuations of the trapped microsphere via the equipartition theorem (Eq. 3.1):

$$\kappa = \frac{k_B T}{< x^2 >} \tag{3.8}$$

where k_B is the Boltzmann constant, T is the absolute temperature and $< x^2 >$ is the variance of the microsphere position. Naturally, a calibrated detector is needed. Also, the detection bandwidth should be large enough to avoid low-pass filtering the measurements so not to overestimate the trap stiffness. An advantage of equipartition calibra-

tion is that it is independent of the shape of the trapped particle as long as its position is detected accurately. The disadvantage of using the equipartition method is that the variance is a biased estimator since it is always positive; noise such as drift and electrical noise inflate the variance and thus lower the calculated stiffness. Another statistical analysis— a more informative one—is to map the trapping potential well. The distribution of the trapped microsphere in a harmonic potential is described by the Boltzmann distribution:

$$p(x) = p_0 e^{-U(x)/k_B T} = p_0 e^{-\kappa x^2/k_B T} \tag{3.9}$$

where $p(x)$ is the probability of the microsphere position, p_0 is a constant and $U = \frac{1}{2}\kappa x^2$ is the potential energy of the trap. The trap stiffness is computed by taking the logarithm of Eq. 3.9 and solving for κ [69].

It is also possible to calibrate the trap stiffness by applying a known drag force on the trapped microsphere. If the sample is moved with a velocity v using the piezo stage, then a drag force is applied on the trapped microsphere, $F_{drag} = v_d \gamma$ where γ is the drag coefficient. The drag force is balance by the trapping force and thus the stiffness is:

$$\kappa = \frac{\gamma v}{x} \tag{3.10}$$

The drag method requires a calibrated detection and the knowledge of the drag coefficient.

The standard calibration method in optical tweezers is the power spectral analysis of the Brownian motion of the trapped microsphere. The power spectral density (PSD) of a trapped microsphere in a harmonic potential as a function of frequency f is ([38], Fig. 3.10):

$$P(f) = \frac{D}{2\pi^2(f_c^2 + f^2)} = \frac{k_B T}{2\gamma\pi^2(f_c^2 + f^2)} \tag{3.11}$$

where D is the diffusion coefficient. The Einstein-Stokes relation for spherical particles in a fluid with low Reynolds number was used, $D = k_B T/\gamma$. f_c is the corner frequency. The PSD is fitted with a Lorentzian that returns a plateau value S_0 and the corner frequency with high precision (Fig. 3.10). From the corner frequency the stiffness can be readily calculated, $f_c = \kappa/2\pi\gamma$, provided that the drag coefficient is known. Here, the detection need not to be calibrated. In fact, it is possible to calibrate the detector from

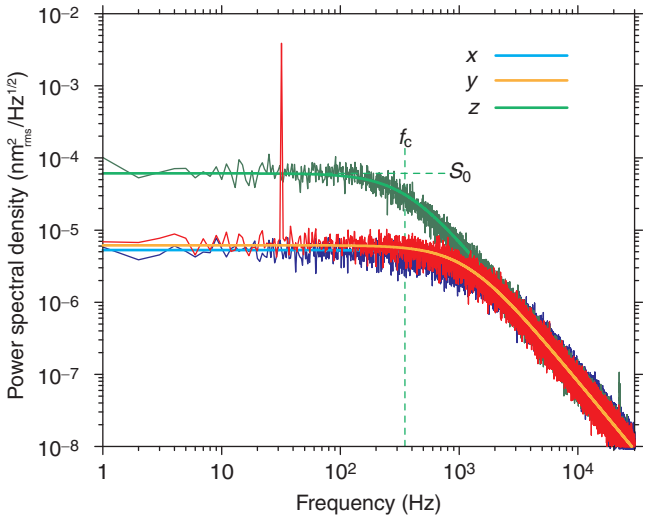

FIGURE 3.10 OPTICAL TRAP CALIBRATION - Example of a calibrated power spectral density of a trapped 0.528 μm microsphere for x-, y-, and z- directions. The calibration spike on the y-direction at $f_{stage} = 32$ Hz results from oscillating the stage at the same frequency. Each power spectrum is an average of 40 independent spectra. The vertical dashed line indicates the corner frequency f_c and the horizontal dashed line indicates the plateau S_0 for the axial direction. The sampling rate was 102400 Hz at a resolution of 1 Hz. Each spectrum is fitted with a Lorentzian (bright lines).

the PSD:

$$\beta = \sqrt{\frac{k_B T}{\gamma D_v}} \tag{3.12}$$

where $D_v = 2\pi^2 S_0 f_c^2$ is the measured diffusion coefficient in units of V^2/s . So with a single measurement, it is possible to calibrate the detector and the trap stiffness. Another advantage of the PSD method is its sensitivity; effects of noise, misalignment, degraded laser profile, etc, cause the PSD to deviate from a Lorentzian, thus, serving as a diagnostic tool as well ([69], Sec. 3.1.4).

The drag and the PSD methods depend on the knowledge of the drag coefficient which is usually calculated via the Stokes relation, $\gamma = 6\pi\eta r$, where η is the viscosity of the surrounding medium, and r is the radius of the microsphere. Uncertainties in the viscosity and in the microsphere size are inherited to the drag coefficient. In addition, the drag coefficient depends on the proximity to nearby surfaces which is the case for surface assays in single beam optical tweezers. Meaning, that for an accurate measurement the drag needs to be measured along with the detector sensitivity and the trap stiffness.

In our setup we used a combined drag force-power spectral method that does not need but does measure the drag coefficient as well as the trap stiffness, the sensitivity factor and the microsphere radius with high accuracy (3%, [22, 70]). Here, the piezo stage is oscillated sinusoidally at a frequency f_{stage} with an amplitude in the range of 500–1000 nm. Due to the oscillations, the trapped microsphere experience additional motion besides the Brownian motion. When measuring the power spectrum of the trapped microsphere an additional peak is observed at the stage oscillation frequency. The amplitude of this "calibration" peak serves as a scale from which the sensitivity factor is measured [70]:

$$\beta = A\left(2P_{spike}\Delta f\left[1+(f_c/f_{stage})^2\right]\right)^{-\frac{1}{2}} \tag{3.13}$$

Where A is the amplitude of the oscillations, $P_{spike}\Delta f$ is the measured power in the spike. With the sensitivity factor known, the drag coefficient is found from Eq. 3.12 and the trap stiffness flows from $f_c = \kappa/2\pi\gamma$. In addition, since the drag coefficient is precisely measured, it is possible to measure the flow cell surface position relative to the microsphere center. We calibrate the trap as a function of distance from the surface [22]. The measured lateral drag can is fitted with Faxen's low from which the position of the surface can be found with nanometer precision. Also, since the temperature is measured, the viscosity can be calculated and so the microsphere radius can be determined using the Stokes relation.

Chapter 4

Under-filling trapping objectives optimizes the use of the available laser power in optical tweezers

When using optical tweezers for biological studies, optimizing the trapping efficiency reduces photo damage or enables the generation of larger trapping forces. One important, yet not-well understood, tuning parameter is how much the laser beam needs to be expanded before coupling it into the trapping objective. We measured the trap stiffness for 0.5-2μm-diameter microspheres for various beam expansions. We show that the highest overall trapping efficiency is achieved by slightly under-filling our high-numerical aperture objective when using microspheres with a diameter corresponding to about the trapping-laser wavelength in the medium. The optimal filling ratio for the lateral direction depended on the microsphere size, whereas for the axial direction it was nearly independent. Our findings are in agreement with Mie theory calculations and suggest that apart from the choice of the optimal microsphere size, slightly under-filling the objective is key for the optimal performance of an optical trap.

4.1 Introduction

When building optical tweezers one eventually needs to decide how much the trapping laser is expanded relative to the size of the trapping objective. If the expansion is too small, the laser focus is not diffraction-limited resulting in smaller stabilizing gradient forces and thus a weaker trap. On the other hand, if the expansion is too large, too

much laser power is truncated resulting also in a weak trap. Therefore, there must be an optimal laser expansion to maximize the trap stiffness for a given laser power. Apart from the laser expansion and choice of a high-numerical aperture (NA) objective, the trapping efficiency can also be optimized by using different beam profiles, for instance, a "doughnut" mode [71] or using anti-reflection–coated microspheres [72, 73].

Although choosing the optimal expansion is key for making the best use out of the available laser power, previous studies give contradicting recommendations. According to calculations based on ray-optics [24, 54] one should slightly *overfill* the objective. Kim *et al.* [74] measured an optimal "laser beam radius-to-the aperture radius" of 1.2 for 5 μm-diameter microspheres in agreement with the ray-optics predictions. In contrast, Bing-Huan *et al.* [75] measured an optimal "effective NA relative to the objective aperture" of 0.7 for 2 μm-diameter microspheres. Recently, Samadi and Reihani [76] measured the optimal "ratio of the beam to the objective's entrance aperture diameter" of about 0.7 for micron-sized microspheres, thus, also recommending *under-filling*. Discrepancies between the studies are due to (i) numerous definitions for the ratio of the beam diameter to some measure of the objective, (ii) different criteria for efficiency (escape force or trap stiffness), (iii) varying microsphere diameters, and (iv) a lack of rigorous Mie theory calculations necessary for particle sizes comparable to the wavelength of light.

Here, we address these points to clarify and reconcile the above-mentioned discrepancies. In addition, we provide information on the axial direction scarcely dealt with previously. Foremost, we introduce a *filling-ratio* parameter which is independent of the objective-back-opening size. The visible stops and apertures in the back of an objective maybe larger than the NA of the objective and furthermore depend on the manufacturer. Therefore, we base our filling-ratio parameter on Abbe's sine condition. All high-quality microscope objectives are designed according to this condition to prevent spherical aberrations and coma. Essentially this means that the first principal plane of the objective is a hemisphere (H_1 in Fig. 4.1a). Light rays emerging from the focus under an angle θ relative to the optical axis leave the back of the objective (on the image side) at a radius $r = nf\sin\theta$ where n is the refractive index of the lens and f is the focal length of the objective obtained by dividing the manufacture's tube length by the magnification of the objective. Note that for large values of θ, common for high-NA objectives, this radius significantly differs from the one obtained with a straight principle plane (for a straight principal plane the radius would scale with $\tan\theta$). Using the definition $\mathrm{NA} = \mathrm{n}\sin\theta$, the marginal rays that corresponds to the NA of the objective thus span the diameter $D_{\mathrm{NA}} = 2f\mathrm{NA}$. This diameter in microscopy is also called the exit pupil. Therefore, we

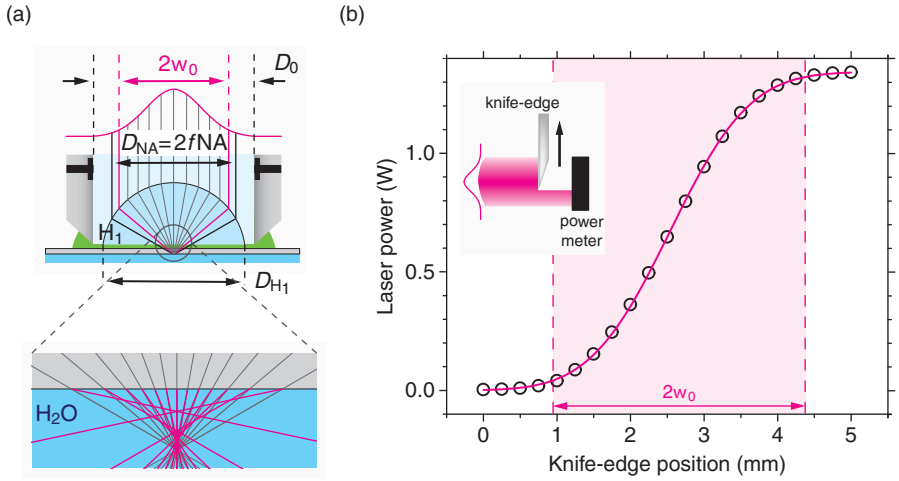

FIGURE 4.1 FILLING RATIO AND LASER PROFILE MEASUREMENT - (a) Schematic objective with a hemispherical principal plane H_1. Zoom: aberrations occurring at a glass-water interface when using oil-immersion objectives. The marginal rays correspond to NA $\approx$ 1.3, the next ones (spaced by 10°) to NA $\approx$ 1.15. (b) Exemplary laser profile measured by the knife-edge method. The power measurements (symbols) were fitted with an error function of width $\omega_0 = 1.71 \pm 0.01$ mm. Inset: schematic drawing of the knife-edge method

define the filling ratio α based on this diameter as

$$\alpha = \frac{2\omega_0}{D_{\mathrm{NA}}} = \frac{\omega_0}{f\,\mathrm{NA}} \tag{4.1}$$

where ω_0 is the laser beam radius at which the intensity decreases to e^{-2} of the central value. If α is multiplied by the NA of the objective, an effective NA can be assigned to the laser beam expansion. This effective numerical aperture in particular the optimal value of it, $\mathrm{NA_{opt}}$ is a dimensionless parameter which can be used to compare the performance of different objectives. Here, we determined the optimal filling ratio and thus $\mathrm{NA_{opt}}$ for microsphere sizes in the range of 0.5–2 μm using an oil-immersion objective (NA = 1.3) and compared the results to Mie theory calculations. As criterion for α, we measured the central trap stiffness since—contrary to the escape force—it is independent of the non-linear trapping force field . We show that slightly under-filling the objective, in our case with $\mathrm{NA_{opt}} \approx 1.25$, resulted in the highest trapping efficiency for both lateral and axial directions.

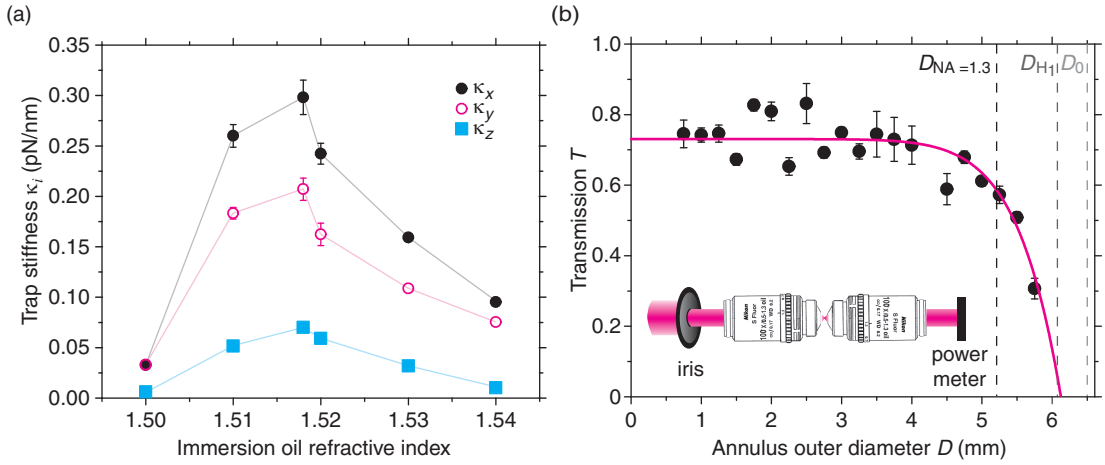

FIGURE 4.2 IMMERSION OIL AND OBJECTIVE TRANSMISSION CONTROLS - (a) Trap stiffness as a function of immersion-oil refractive index for 0.46 μm-diameter microspheres. (b) Objective transmission through an annulus with outer diameter D centered on the optical axis. The line is a fit using $T = T_0 - aD^{10}$ with $T_0 = 0.73$ and $a = 10^{-8}\,\mathrm{mm}^{-10}$. Inset: Schematic of the measurement (see text for details). For (b) and (c) each symbol is the mean of three measurements. Error bars are standard deviations plotted only if larger than the symbol size.

4.2 Controls and Methods

4.2.1 The optimal immersion oil and uniform objective transmission ensured diffraction-limited performance

Immersion oil. We determined the optimal refractive index of the immersion oil for trapping close to a surface. Reihani and Oddershede [57] reported that an immersion oil with a refractive index of $n = 1.518$, index-matching the cover slip, reduced their trapping efficiency. This was especially the case when working close to the cover glass surface using a NA = 1.32 oil-immersion objective. Using higher refractive-index oils increased their trapping efficiency because spherical aberrations were compensated. Therefore, we measured the trap stiffness as a function of immersion-oil refractive index (Fig. 4.2a). We varied the refractive index in the range of 1.5–1.54 in increments of 0.01 (Series A; Cat.-#. 18095; Cargille Laboratories, NJ, USA) including the standard oil we typically use (Immersol, $n = 1.518$; ZEISS, Germany). For all directions, the trap stiffness peaked at the standard oil showing that it is indeed the optimal immersion oil for our setup.

Trapping objective transmission. To compare our measurements with the calculations, we measured the infrared transmission of the trapping objective. This measure-

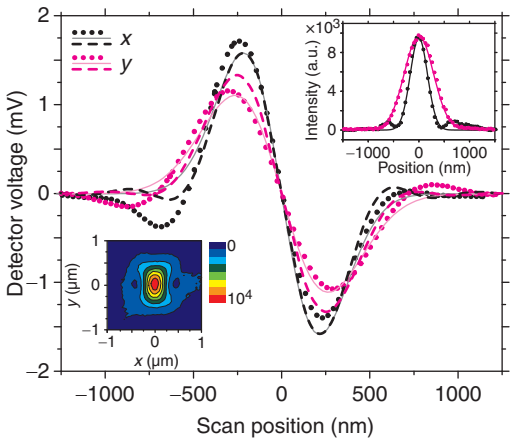

FIGURE 4.3 LASER FOCUS PROFILE ($\alpha = 0.95$) - Scans (dotted lines) through 80 nm-diameter gold particles fitted to the derivative of a Gaussian ($\omega_{x(y)} = 410(530)$ nm; dim solid lines) and compared to our calculations ($\omega_{x(y)} = 400(470)$ nm; dashed lines). The insets show a CCD image of the laser focus and cross-sections (dotted lines; both in the same units) through the center fitted by Gaussians ($\omega_{x(y)} = 340(570)$ nm; lines)

ment enabled us to calculate the power in the laser focus and account for a potentially non-uniform transmission [77]. Using the two-objective method, we measured the laser transmission as a function of distance from the optical axis (see inset Fig. 4.2b) [77]. We incremented the diameter of a calibrated iris by 0.25 mm. For each increment i, we measured the power before, P_{before}, and after, P_{after}, the identical objectives. We then calculated the transmission of a single objective through an annulus of outer diameter D_i according to $T(D_i) \approx ([P_{\text{after}}(D_i) - P_{\text{after}}(D_{i-1})]/[P_{\text{before}}(D_i) - P_{\text{before}}(D_{i-1})])^{\frac{1}{2}}$. The central transmission was 73 % in very good agreement with the manufacturer's specification (Fig. 4.2b). Also, the transmission was nearly constant up to the diameter corresponding to the objective NA (exit pupil) of $D_{\text{NA}} = 5.2$ mm. For larger diameters, the transmission dropped rapidly and was zero at ≈6.12 mm in agreement with the principal-plane diameter $D_{\text{H}_1} = 2n_{\text{oil}}f = 6.07$ mm. The visible stop in the back of the objective had a diameter of $D_0 \approx 6.5$ mm (see Fig. 4.1a). Thus, the objective back opening was much larger (about 25 %) compared to the corresponding NA or pupil diameter. Note that significantly smaller filling ratios result when this stop is used as a reference.

Laser focus. Since our trapping objective is not optimized for the near-infrared, we measured the laser profile in the focal plane to ensure diffraction-limited performance (Fig. 4.3). We took a camera image of the laser focus reflected from the glass-water interface. In addition, we scanned through gold nanoparticles and recorded the profile with

the QPD. Both measurements we compared with the profiles used in the trap stiffness calculations. The measured profiles were asymmetric as expected for a linearly polarized laser and approximately agreed with the calculated size. The beam radius obtained from the gold-nanoparticle scans were 3 % (13 %) larger compared to the theoretical values used in the calculations for the $x(y)$-direction, respectively. We expected this difference because the laser beam is not a perfect Gaussian beam as characterized by the so-called M^2 value. The diffraction-limited spot size is proportional to this M^2 value. According to the specifications of our laser, $M^2_{x(y)} = 1.05(1.13)$ for the $x(y)$-direction, respectively. These values account for the increase in the measured spot size. As an independent visual control, we recorded an image of the laser focused on the cover slip surface. The size determined from cross-sections through the image were 15 % smaller (21 % larger) relative to the theoretical values for the $x(y)$-direction, respectively. We attribute these differences to polarization effects: before the light reaches the camera it passes a dichroic mirror and several other optics which may have a polarization-dependent transmission. In addition, the camera sensitivity may be polarization-dependent. There were no such uncertainties for the gold-particle scans. Therefore, we assume that the size obtained from the latter data reflect the true size of our laser focus. Taken together, the objective performed nearly diffraction-limited.

4.2.2 Sample preparation, trap calibration and laser profile measurements

The sample was made of two cleaned cover slips ($18\times18\,mm^2$ and $22\times22\,mm^2$, No. 1.5; Corning, NY, USA) glued together by two pieces of double-sided tape leaving a channel of $18\times3\times0.1\,mm^3$ in size. The channel was filled with an aqueous solution of polystyrene (PS) microspheres (Bangs Laboratories, Fishers, USA) containing 1 mM KCl. The salt screens repulsive surfaces forces to less than 100 nm [22] such that microspheres can get into close proximity of the surface but do not get immobilized by the attractive van-der-Waals interactions. To prevent evaporation, the sample was sealed with nail polish.

To measure the trap stiffness we used the calibration method described in Sec. 4.2. For every microsphere, we measured all parameters as a function of microsphere–cover-slip distance at ≈50 positions starting from a distance of about 3 μm until the microsphere touched the surface. From the distance dependence of the drag coefficient, we determined the cover-slip surface position with nanometer precision. For this position, we state the determined trap stiffness [22]. We calibrated at least six different micro-

spheres for each size and filling ratio.

To determine the filling ratio, we measured the laser beam radius ω_0 directly before the objective in both the x- and y-direction using the knife-edge method [78] (Fig. 4.1b). All profiles had a Gaussian shape.

4.3 Results and Discussion

4.3.1 Under-filling resulted in the highest trap stiffness

To determine the optimal filling ratio, we measured the trap stiffness (see Sect. 4.2) as a function of the filling ratio for four microsphere diameters (0.46, 0.85, 1.01, and 2.01 μm) and seven filling ratios ($\alpha \approx 0.54$, 0.67, 0.82, 0.96, 1.15, 1.66 and 2.25) using a constant laser power before the trapping objective (Fig. 4.4). From the measurements we can draw the following conclusions: (i) The trap stiffness—for both the lateral and axial directions—was largest at a filling ratio below one, i.e. at under-filling conditions, for all microsphere sizes. (ii) For the lateral directions, the optimal under-filling ratio was size-dependent and decreased with increasing microsphere diameter. For example, the optimal filling ratios for the x-direction were 0.94, 0.94, 0.8 and 0.66 for the four different microsphere sizes, respectively. (iii) For the axial direction, the optimal under-filling ratio was rather size-independent and about 0.95. (iv) As expected [72], the overall highest trap stiffness was achieved with the microspheres that had a diameter of 0.85 μm. This diameter corresponds to about the trapping laser wavelength in the medium, $\lambda/n_{\text{medium}} \approx 800$ nm, where a Mie resonance occurs [27]. During the measurements, we noticed that with filling ratios $\alpha \lesssim 0.9$, the trapping of microspheres became more difficult and the distance from the surface up to which microspheres could still be trapped decreased (to about 5 μm from the cover-slip surface for $\alpha = 0.67$). This effect is due to the low effective NA and the increasing offset between the trap center and the focus (see below and inset Fig. 4.4c). With increasing distance to the surface, spherical aberrations increase. This increase weakens the trap until microspheres cannot be trapped anymore. At the lowest filling ratio of $\alpha = 0.54$ corresponding to an effective NA of 0.7, we were not able to trap any microspheres anymore because the gradient force in the axial direction was too small compared to the scattering force. In summary, the optimal laser expansion depended on the experimental choice of the microsphere size.

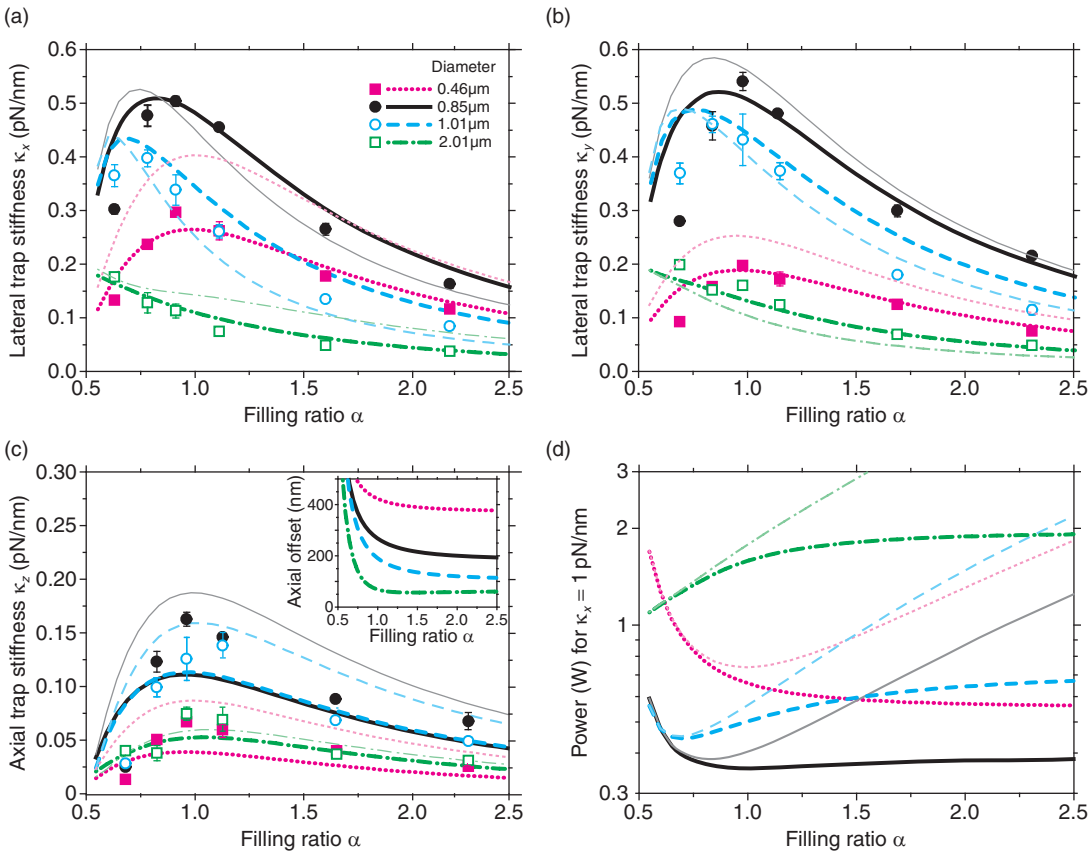

FIGURE 4.4 TRAP STIFFNESS AS A FUNCTION OF THE FILLING RATIO - Trap stiffness measurements (symbols) and calculations (thick [thin] lines for NA = 1.2[1.3]) as a function of filling ratio α for four microsphere sizes in the lateral x- (a), y- (b), and axial z-direction (c). Inset in (c): Axial trap position relative to the center of the focus as a function of filling ratio (NA = 1.2). Symbols are averages obtained from ≥6 different microspheres for each size. Error bars are standard deviations plotted only if larger than the symbol size. For all measurements the laser power before the trapping objective was $P = 250\,\mathrm{mW}$. Due to a 4 % asymmetry in the laser profile, overfilling ratios in the $y-$axis were slightly larger than those in the x-axis. (d) To achieve a trap stiffness of $\kappa_x = 1\,\mathrm{pN/nm}$, the power in the focus (using our fit parameters; thick lines [NA = 1.2]) and before the objective (assuming 100 % transmission; thin lines [NA = 1.2]) are plotted as a function of α.

4.3.2 Mie theory calculations confirm the under-filling optimum

To compute the trap stiffness, we calculated the light momentum transfer onto the microspheres based on the generalized Lorenz-Mie theory. To this end, we used and extended the optical tweezers computational toolbox [35] to account for (i) the filling ratio, (ii) the spherical principal plane, (iii) the transmission profile of the objective, and (iv) the

change in light-ray angles due to the glass-water interface. The latter was implemented based on Snell's law and is approximately valid for water-immersion objectives. A full treatment of aberrations in the case of oil-immersion objectives is not implemented. A detailed description of the modifications to the MATLAB® scripts is provided in the end of this section.

We found qualitative agreement between theory and experiment in terms of how the trap stiffness depended on the filling ratio, microsphere size, polarization, and trapping direction. This agreement confirms the experimental conclusions above. The thick lines in Fig. 4.4 were obtained with the following parameters: PS microspheres with a refractive index $n_{\mathrm{PS}} = 1.57$ trapped in water, $n_{\mathrm{medium}} = 1.326$, with 1064 nm-light polarized in the y-direction truncated at an angle corresponding to an effective NA of 1.2. For this global fit, we varied only two parameters: the truncation angle, i.e. the effective NA of the objective, and a scaling factor for the effective power in the focus. We found that the effective NA was smaller compared to the oil-immersion objective's specification due to spherical aberrations at the glass-water interface (zoom Fig. 4.1a). The theoretical power was significantly lower (scaling factor of 0.62) than our measured power in the focus. To show how the NA affects the shape of the trap stiffness curves, we also calculated the trap stiffness for the objective NA of 1.3 using the same scaling factor of 0.62 (thin lines). The calculations for NA = 1.3 deviated significantly more than the ones for NA = 1.2 indicating that the effective NA of our objective was reduced by the spherical aberrations at the glass-water interface.

Scaling of the trap stiffness with respect to all other parameters agreed qualitatively with the theory, whereas the scaling with power did not. The origin of this discrepancy is unclear, but was observed before [72]. In our present work, we tried to rule out efficiency losses due to (i) the immersion oil (Fig. 4.2a), (ii) the objective transmission (Fig. 4.2b), (iii) a lack of diffraction-limited performance of the objective (Fig. 4.3), and (iv) calculated power loss in the focus due to diffraction (<15% for $\alpha = 2.5$, [30]). Note that the power in the focus is deduced from the transmission measurements and not directly measured. How much spherical aberrations from the glass-water interface affect our measurements is unclear as well. Since we work close to this interface ($\lesssim 3\,\mu$m distance where we measured the trap stiffness), we do not expect that these aberrations fully account for the large difference between theory and experiment [79]. Our measurements, scaled properly, are comparable to other trap stiffness measurements obtained with a water-immersion objective [80]. Whether quantitative agreement between theory and experiments using the optical tweezers computational toolbox can be achieved with an

infrared-corrected water-immersion objective is therefore unclear. We do not know of any report that tested the toolbox quantitatively against an optical trapping experiment.[¶]

While the overall data, apart from the power scaling, qualitatively agreed with the calculations, there were some systematic deviations which we attribute to the aberrations induced by the glass-water interface. These aberrations broaden the focus with increasing surface distance and more so with respect to the axial compared to the lateral direction [79]. Therefore, we expected and observed larger differences between theory and experiment for the axial trap stiffness (Fig. 4.4c). Furthermore, we consistently measured smaller trap stiffness values compared to the theory for small filling ratios. This effect arises because the offset between the axial equilibrium trap position and the laser focus strongly increases for $\alpha < 1$ based on our calculations (inset Fig. 4.4c). This increase is exacerbated by the aberrations mentioned above with the consequence of a systematic weakening of the trap. Overall, our error bars on the trap stiffness measurements were smaller than the mean deviation from the theory, however, considering that with each filling ratio the complete laser path, and with each sample the condenser objective and detector had to be re-aligned, the overall agreement for the range of microsphere sizes and filling ratios is remarkable.

Modifications to the toolbox scripts

To calculate the trap stiffness, we modified the script "bsc_pointmatch_farfield" of the optical tweezers computational toolbox [37]. This script calculates the vector-spherical-wave-functions expansion coefficients of the laser at the focal plane by matching it to a laser profile in the far field. The electrical field E for a radially symmetric profile is expressed in terms of an incoming angle θ instead of a radial coordinate r in accordance with Abbe's condition (see Introduction). Using our definition of the filling ratio (Eq. 4.1), we obtain

$$E = \exp\left(\frac{r}{\omega_0}\right)^2 = \exp\left(\frac{2 f n_{\text{medium}} \sin\theta}{\alpha D_{\text{NA}}}\right)^2 \tag{4.2}$$

where θ is in the range of 0–π. Note the usage of the medium refractive index to account for the glass-water interface. To implement laser power losses due to truncation by the objective, the trap stiffness is reduced by multiplying with a power normalization factor

$$P_{\text{trunc}} = T_0 \left[1 - \exp\left(-2\left[\frac{D_{\max}}{\alpha D_{\text{NA}}}\right]^2\right)\right] \tag{4.3}$$

[¶]Note that version 1.0 of the optical tweezers computational toolbox contained a power scaling error in the code which was corrected in version 1.1.

assuming a constant transmission T_0 where $D_{\max}$ is the largest diameter up to which light is still transmitted. Since we measured the transmission of the objective, we multiplied the Gaussian beam with the fitted transmission curve and integrated the intensity up to the diameter of the principal plane. This changed P_{trunc} slightly compared to the above equation.

4.4 Conclusions

For all microsphere sizes, both experiment and calculations show that slight under-filling the objective maximizes the use of the available laser power. At under-filling conditions less power is truncated at the cost of a wider focus due to a lower effective NA. The calculated trap stiffness is the product of the trapping efficiency with the power in the focus. Since the maximum in trap stiffness occurs at under-filling conditions it means that the power loss due to truncation has a stronger dependence on the filling ratio than the increase in trapping efficiency with respect to a tighter focus. This is expected because power truncation exponentially depends on α (see Eq. 4.3) and therefore the effective NA, while the diffraction-limited spot size scales only inversely with the effective NA. One direct consequence of optimizing trapping efficiencies is the reduction of heating and photo-damage in particular when working with biological samples. The least power in the focus to generate a trap stiffness of 1 pN/nm was needed for the 0.85 μm-diameter microspheres for $\alpha = 1$ ($\approx$360 mW based on our calculations, black solid line Fig. 4.4d). For the 0.46 μm-diameter microspheres, the power to achieve the same trap stiffness was at least 50 % larger (thick magenta dotted line). The larger the over-filling ratio was for this size, the less power in the focus was necessary. This trend was contrary to the other microsphere sizes we used. For the two large microsphere sizes we tested, under-filling conditions lead to the least power for a 1 pN/nm-trap. When designing optical tweezers, Fig. 4.4d may also serve as a reference for how much output power the laser needs to have. For $\alpha \gtrsim 1$, truncation leads to significant power loss (thin lines). The truncated power may lead to additional heating and thermal drift of the objective [81].

In the light of our results, we can return to the different filling ratio recommendations found in the literature. Using our filling ratio definition (Eq. 4.1), Kim *et al.* [74] measured a rather large optimal $\alpha \approx 1.7$ due to aberrations (usage of an oil-immersion objective and trapping $\approx$25 μm away from the surface without refractive index compensation). The optimal value of $\alpha = 0.83$ ($\text{NA}_{\text{opt}} = 1.12$) from Bing-Huan *et al.* [75] is still large compared to our 2 μm-diameter-microsphere measurements. Samadi and Reihani's [76] optimal measured ratio of 0.65 for 0.8 and 1.0 μm-diameter microspheres corresponds to

an optimal NA_{opt} of 1.14 and $\alpha = 0.88$ in good agreement with our measurements. Thus, using a reference parameter for the filling ratio which is independent of the objective's back opening size helps in comparing different studies.

For a general, all-purpose usage of the optical tweezers, we recommend a filling ratio slightly below one of $\alpha_{opt} \approx 0.95$ when using a 1.3 NA–oil-immersion objective. This value corresponds to an optimal filling numerical aperture of $NA_{opt} \approx 1.25$. According to our calculations the optimal values for the lateral directions were lower ($\alpha \approx 0.8$, $NA_{opt} \approx 1.04$). Therefore, we expect that optimal values for water-immersion objectives with minimized spherical aberrations are lower, in particular for objectives corrected in the near-infrared. As total-internal-reflection-fluorescence (TIRF) objectives are used with immersion oils, we expect that spherical aberrations reduce the effective NA to values comparable to our measurements. Any light rays at radial distances corresponding to NAs larger than the refractive index of the trapping medium cannot contribute to the trap because of total internal reflection. Thus, for TIRF objectives with NA $\geq$ 1.4, optimal under-filling ratios should be less than 0.9 based on $NA_{opt} \approx 1.25$.

Chapter 5

Temperature-controlled objectives with millikelvin precision to reduce drift and maintain base-pair resolution

Thermal drift is detrimental for high resolution measurements. In particular, absorption of the trapping laser light by the microscope objective that focuses the beam leads to heating of the objective and subsequent drift. This entails long equilibration times which may limit sensitive biophysical assays. We implemented an objective temperature feedback system for minimizing thermal drift. We measured that the infrared laser heated the objective by 0.7 K per watt of laser power and that the laser focus moved relative to the sample by 0.1 nm / mK due to thermal expansion of the objective. The feedback stabilized the temperature of the trapping objective with millikelvin precision. This enhanced the long-term temperature stability and significantly reduced the settling time of the instrument to about 100 s after a temperature disturbance while preserving the resolution of the setup.

5.1 Introduction

Optical tweezers with back-focal-plane detection have sub-nanometer precision on time scales shorter than 1 s. In contrast, on time scales longer than ≈1 s, nanometer movements are often caused by instrumental noise in particular thermal drift as discussed

in Chapter 3. To achieve sub-nm resolution on long time scales for high-resolution measurements of DNA-protein interactions, differential measurements have been developed either in form of dual-trap assays decoupled from surfaces [5, 17, 82] or by active tracking of a fiducial mark for surface-coupled assays [23]. Differential measurements reduce noise because drift affects both recorded positions nearly equally and can thus be subtracted. Absolute measurements of surface-coupled assays have achieved sub-nm resolution by employing a simple, mechanically stable instrument and minimizing laser intensity fluctuations and pointing stability [22].

Experimental procedures during trapping assays involve changes in laser intensity, for example, in form of closing a shutter to trap a new particle or due to changes in trap stiffness [18, 45]. For infrared lasers, such intensity changes lead to a significant change in heating of the trapping objective [54]. Since thermal relaxation times of the objective and more importantly its mount are on the order of several 100–1000 s—as we will show below—long equilibration times are needed to regain stable conditions. Such long times are often not desirable in sensitive single molecule biophysical assays. To reduce equilibration times, active temperature stabilization is necessary. Commercially available objective heaters provide temperature stability to within 0.1 K at best. Objective heating by fluid-pumped copper jackets reached similar temperature stability [83]. Such a temperature range leads to approximately 100 nm expansion of an objective based on a linear thermal expansion coefficient of $\approx 20 \cdot 10^{-6}\,\mathrm{K}^{-1}$ and an objective size of ≈5 cm. This expansion directly shifts the focal point of the objective relative to the sample and therefore leads to drift of the optical tweezers relative to the surface. Thus, to achieve nm-resolution for absolute measurements, the objective temperature needs to be stabilized with millikelvin precision.

Here, we implement an objective temperature heating system based on Pt100 resistance temperature detectors and heating foils which are controlled via custom-written software using LabVIEW. We achieve millikelvin precision with about 8 s response time of the temperature feedback. By tracking immobilized microspheres on surfaces, we demonstrate the overall performance of the feedback and the detrimental heating effects that the laser has.

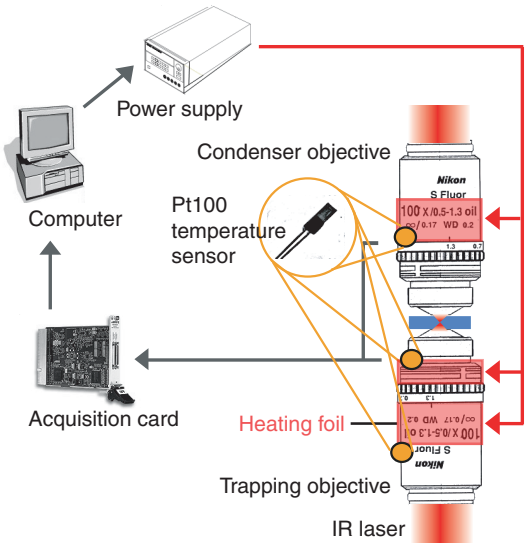

FIGURE 5.1 TEMPERATURE FEEDBACK - Schematic drawing of the temperature feedback. The red bands around the objectives indicate approximately the position and size of the heating foils.

5.2 Materials and Methods

5.2.1 Implementation of the temperature feedback

The core elements of the temperature feedback are Pt100 temperature sensors attached to the objective and the condenser, heating foils wrapped around the objectives to give uniform heating, and a standard, software-based PID controller programmed in LabVIEW [Fig. 5.1]. To ensure proper contact of the sensors and foils with the objectives, we used thermal conducting paste or glue. The heating foils (Minco SA, Aston, France) were connected to a power supply (E3631A Agilent, Santa Clara, USA) which communicated with the computer via an RS232 connection. The resistance of the sensors (class 1/3B) are measured in a three-wire configuration using standard electronics (PXT-10, Brodersen, Mülheim/Ruhr, Germany), digitized by a data acquisition card (NI PXI-6621, National Instruments, USA), and converted to temperature using the Callendar-Van Dusen equation. The temperature is measured every 0.25 s and the heat foil voltage updated accordingly. Additionally, we monitored the temperature of the microscope and the room. The sensors had an accuracy of ≈0.15 °C and a sub-mK precision.

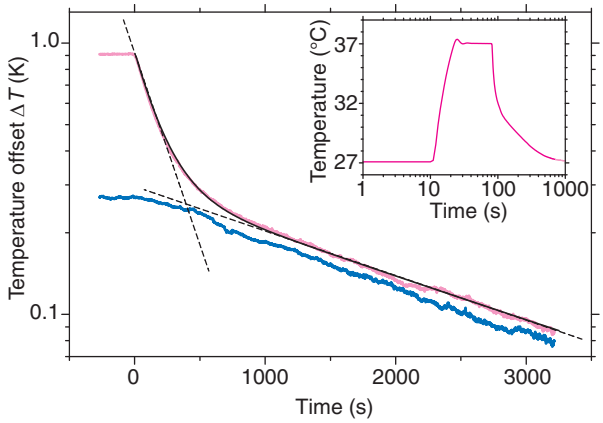

FIGURE 5.2 LASER HEATING OF THE OBJECTIVE - Objective temperature deviation (—) above the final, equilibrium temperature as a function of time. At time zero the shutter was closed. The relaxation was fitted by a double exponential decay (—) that returned $\tau_o = 190\,s$ and $\tau_m = 2600\,s$ attributed to the objective and microscope, respectively. Guides to the eye (- - -) indicate the fast and slow relaxation. Concurrently, the microscope temperature (—) decreased slowly. The laser power was ≈1.4 W at the back aperture of the objective, the starting temperature was 27.50 °C, and the final temperature was 26.58 °C. Inset: Objective temperature reached a 10 °C higher set point temperature after ≈10 s using the temperature feedback. Return to the previous set point was slower.

5.2.2 Sample preparation

The sample is made of two cleaned cover slips ($18\times18\,mm^2$ and $22\times22\,mm^2$, No. 1.5, Corning, NY, USA) glued together by two pieces of double sticking tape. The separation caused by the tape forms a channel $18\times3\times0.1\,mm^3$ in size with a volume of ≈5 µl. The channel was filled with an aqueous solution of 530 nm-diameter polystyrene microspheres (Polysciences, Warrington, USA) containing 0.1 M KCl and sealed with nail polish. The salt screened the electrostatic repulsion and resulted in surface-immobilized microspheres [22].

5.3 Results

5.3.1 Significant laser heating and slow relaxation

How much does the laser heat the objective and how long does it take to equilibrate? To measure the amount of laser heating without the temperature feedback, we operated the optical tweezers at full power—nominally 2 W laser output reduced to ≈1.4 W at the back aperture of the objective—and let the system equilibrate over night. Then we closed the shutter and recorded the objective and microscope temperature as a function

of time (Fig. 5.2). The objective temperature relaxation was well described by a double exponential fit. We attribute the short relaxation time, $\tau_o = 190\,s$, to the objective and the long one, $\tau_m = 2600\,s$, to the microscope since the slow relaxation approached the microscope temperature. Thus, when the shutter was closed for a long time, the optical tweezers needed at least two hours ($\approx 3\tau_m$) to thermally equilibrate once the laser was turned back on. With an overfilling ratio of 1.3, about 30% of the laser intensity was absorbed at the back aperture of the objective. Using an iris in front of the objective with the same aperture as the latter reduced the amount of objective heating by ≈30% heating the iris instead.* We did not use an iris because it conflicted with beam steering and relaxation times did not shorten when using the iris. To circumvent long equilibration times, we implemented temperature-controlled objectives that are heated a few degrees above room temperature. With the feedback, the heating foils compensate for the loss of laser heating when the laser is turned off maintaining the objectives at a constant temperature.

5.3.2 Optimal temperature sensor and heating foil positions

The position of the temperature sensor and the heating foil played a crucial rule for the performance of the feedback. The shorter the distance between the sensor and the foil, the shorter the lag time of the feedback improving its bandwidth and performance (Fig. 5.3). For optimal heat compensation, the heating foil should ideally be placed where the laser is heating the objective most. However, this position is *a priori* unknown and might not be accessible due to the geometry of the objective. For example, unsuitable positions on our objective were the spring-loaded tip and the adjustment collar for the numerical aperture [see Fig. 5.1]. We mounted one heating foil directly underneath the adjustment collar and one above it. One temperature sensor was placed above the upper heating foil as close as possible to the sample and one below the lower one. We tested two feedback configurations: (i) usage of only the upper sensor controlling the lower heating foil (at a distance of ≈20 mm) with the upper heating foil turned off and (ii) both sensors controlling the heating foil next to them (≈3 mm spacing between sensors and foils). In the latter case, the temperature set point of the lower feedback was 0.25 K lower than for the upper one. This temperature gradient resembled the one created by the laser itself. The standard deviation of the temperature near the sample measured over 1000 s

*This work chronically precedes the work in chapter 4. At the time, we overfilled the objective—according to recommendations. Also, when computing the filling ratio, we divided the laser width by the aperture diameter instead of the exit pupil. Thus the filling ratio was actually 1.6 and not 1.3.

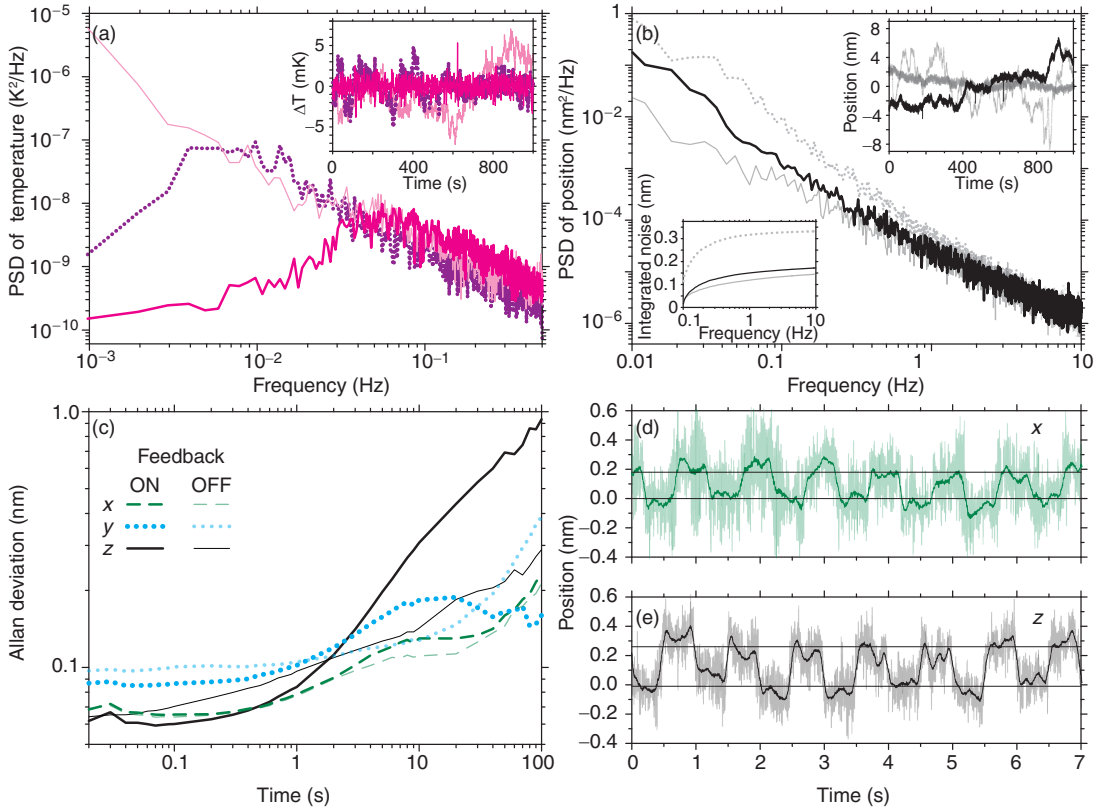

FIGURE 5.3 STABILITY OF OBJECTIVE TEMPERATURE AND IMMOBILIZED-MICROSPHERE POSITION. - (a) Power spectral density (PSD) of the objective temperature for the feedback — OFF, ···· ON with single-, — ON with double-heat-foil configuration. Inset: Deviation of the objective temperature from the mean as a function of time for the feedback. (b) PSD of the axial position for the three cases (— OFF, ···· ON with single-, — ON with double-heat-foil configuration). All PSD curves are an average of 8 spectra. Upper inset: Deviation of the axial position from the mean as a function of time. Lower inset: Integrated positional noise as a function of frequency. (c) Allan deviation of position with the double-heat-foil configuration and without temperature feedback. (d,e) Steps of an immobilized microsphere created by moving the piezo translation stage with $\Delta x = 0.18$ nm in (d) and $\Delta z = 0.27$ nm in (e). Data were acquired with a sampling frequency of 10 kHz and are displayed with 10 Hz (200 Hz, shaded colors) bandwidth obtained by adjacent averaging.

in steady conditions was 2.9, 1.5, and 0.9 mK for the feedback off, the feedback on with one and two operating heating foils, respectively [inset Fig. 5.3(a)]. The response times of the feedback were 32 and 8 s for the single- and double-heating-foil configuration, respectively [Fig. 5.3(a)]. Even though the double-heating-foil configuration performed better with respect to temperature stability and response time, the single-heating-foil configuration resulted in less axial movement of an immobilized microsphere with respect to changes in laser intensity (see Sect. 5.3.5).

5.3.3 Single DNA base-pair resolution with temperature feedback

To judge the performance of the temperature feedback with respect to the positional stability of the optical tweezers, we tracked immobilized microspheres. This is the most stringent test for the setup because it measures fluctuations of both the surface and the laser. The standard deviation of the axial position measured over 1000 s in steady conditions was 0.7, 2.9, and 2.4 nm for the feedback off, the feedback on with one and two operating heating foils, respectively [upper inset Fig. 5.3(b)]. Note that the good value without feedback was only reached after long equilibration times without any disturbance of the room, i.e. not practical every day conditions. The power spectral density (PSD) of the position revealed that the temperature feedback introduced additional noise in the axial direction for time periods longer than ≈1 s. The integrated noise [lower inset Fig. 5.3(b)] for 0.1–10 Hz was below one DNA base pair (0.34 nm—the spacing between subsequent nucleotides) with the double-heating-foil configuration performing nearly as good as without the feedback. Since the magnitude of the integrated noise critically depends on the lower frequency bound, we calculated the Allan deviation (Fig. 5.3(c), [40]) to get a measure of the noise level for all time periods. For periods longer than 1 s, the feedback (two-foil version) introduced additional axial noise compared to no feedback. For the lateral directions, results were comparable to, if not better than, the case without the feedback. Nevertheless, even for the axial direction single base-pair resolution was reached based on the Allan deviation for times shorter than ≈10 s. We directly tested this resolution by moving the stage in a stepwise manner [Fig. 5.3(d,e)]. In both lateral and axial directions, we could resolve steps smaller than a single base pair. Thus, the setup is capable of high-resolution measurements of DNA-protein interactions [17, 82] in a surface-coupled assay [84].

5.3.4 Trap movement correlated with temperature changes

Using the temperature feedback, we measured how much the laser focus moved upon temperature changes. We changed the set point temperature for both objectives in increments of 20 mK about every ≈300 s recording the microsphere position simultaneously (Fig. 5.4). Reversal of the steps also reversed the position of the microsphere. For example, the zero position for the axial direction was revisited to within ≈10 nm after ≈3000 s. For each step, positions were averaged after the transient response of the feedback and plotted against the temperature change (inset Fig. 5.4). Linear fits to the data resulted in 0.07, 0.05 and 1.0 nm/mK movement for x, y and z, respectively. The displacement sensitivity with respect to temperature changes was largest in the axial direction. This,

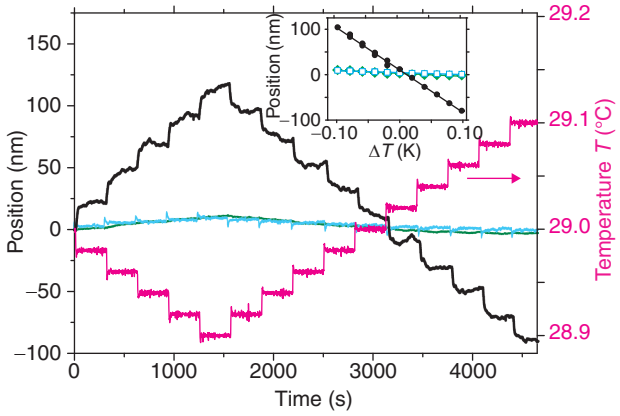

FIGURE 5.4 THERMALLY INDUCED TRAP MOVEMENT - (a) Displacement response of microsphere position (— x, — y, and — z; left-hand axis) to 20 mK steps of the temperature set point (step duration: ≈300 s; — objective temperature T, right-hand axis). Inset: Microsphere position (◇ x, □ y, and • z) as a function of temperature deviation.

we attributed to the thermal expansion of the objective: With the linear thermal expansion coefficient of brass, $19{\cdot}10^{-6}\,\mathrm{K}^{-1}$ multiplied by the size of the objective, 6 cm, we arrive at 1.14 nm/mK which is in good agreement with our measurements. Thus, the heating mainly expanded the trapping objective while all the other components of the optical tweezers remained stationary on the time scale of the experiment. The smaller drift in the lateral directions indicated that heating of the laser and the heating foils was uniform and did not lead to significant bending of the objective.

5.3.5 Feedback restores equilibrium fast

To study the effectiveness of the temperature feedback, we closed the shutter for different time intervals and measured how long the system needed to restore its initial state with and without the feedback (Fig. 5.5). The shutter was closed for various time periods (grey boxes). During the closure time, the laser did not heat the objective. Without the feedback [Fig. 5.5(c)] the temperature decreased depending on the duration of the closure. Surprisingly, even a closure as short as 5 s resulted in ≈20 nm axial movement. The re-equilibration time was ≈200 s. For the 100 s closure, the waiting time increased to more than 20 min with axial displacements of ≈300 nm. In contrast, using the feedback [Fig. 5.5(a,b)] the system re-equilibrated within ≈100 s independent of the closure time. Using the feedback with the single heating foil [Fig. 5.5(a)], the axial position changed by ≈50 nm at most. The drawback of this feedback was the increased positional noise with a slower response time compared to two heating foils. With two heating foils em-

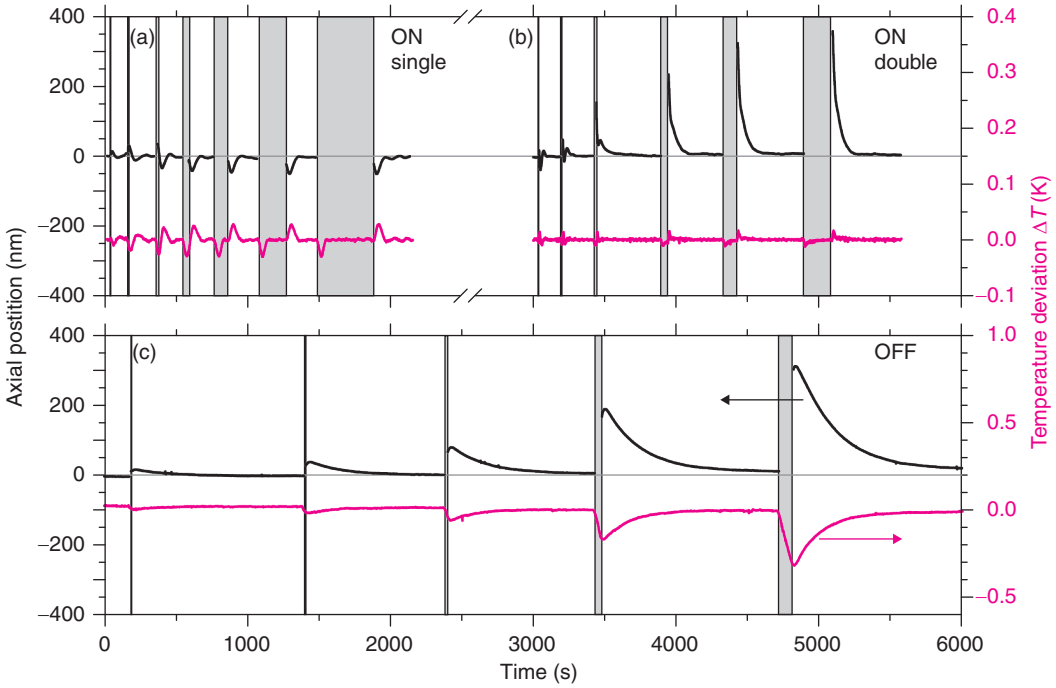

FIGURE 5.5 RESPONSE TO SHUTTER CLOSURE - Axial microsphere position (—) and objective temperature deviation (—) from the equilibrium/set point temperature with temperature feedback ON [(a) single- and (b) double-heating-foil configuration] and OFF (c). Grey boxes represent closure periods (5, 10, 20, 50, 100, 200, and 400 s; not all long closure events are shown). During closures there was no laser reaching the position detector. Therefore, the microsphere position could not be measured leading to discontinuities in the trace.

ployed [Fig. 5.5(b)], the axial movements are comparable to the ones in the absence of the feedback, however, the time needed to re-equilibrate was much faster. The different behavior of the two feedback configurations we ascribed to the unknown heating profile of the laser. While the temperature was locally controlled by the feedback, the overall temperature distribution and thus the average temperature of the objective might be different when the laser or the foils heat the objective. The single-heating-foil configuration resulted in a thermal expansion comparable to the one from the laser, while the two-heating-foils version heated on average less than the laser resulting in a shrinking of the objective when the shutter was closed—a lowering of the focus with an apparent upward movement of the immobilized microsphere.

5.4 Discussion & Conclusion

Our experiments have shown that laser heating of the objective can cause hundreds of nanometers of movements due to thermal expansion and that relaxation times are long. Both aspects are undesirable for sensitive, high-resolution, biophysical measurements. Therefore, we use the two-heat-foil configuration on an everyday basis. Remaining long-term drift we attribute—based on our temperature sensors throughout the laboratory—to the slow temperature cycle of the building, random heat sinks (e.g. opening of a door or the sleep-mode of a monitor), and the presence of extra heat sources in the room such as the human body. Compared to published [83] and commercially available objective heaters we achieved an improved temperature stability. This improvement we ascribe to the long-term stability of the Pt100 elements, the fast response time of the heating foils, the good thermal contact between sensors, foils and the objectives, and, last but not least, to the short distance between the sensors and the foils. Overall this led to the short lag times—i.e. the fast response of the feedback—and ultimately the millikelvin temperature stability.

The feedback improved relaxation times significantly to about 100 s, but introduced some extra positional noise. However, this noise was low enough that steps with a size smaller than a single DNA base-pair could still be resolved in both lateral and axial directions. Together, this improves the throughput of high-resolution experiments without the need of long equilibration times or sacrificing normal shutter usage.

Acknowledgments

We thank Fabian Czerwinski for sharing his MATLAB script to calculate the Allan deviation.

Chapter 6

Conclusions and outlook

Scientific techniques are the tools by which science moves forward. Introduction of new techniques, combining techniques, or optimizing existing techniques is an ongoing process within which the work of this thesis can be categorized. We designed and constructed a high-resolution, single-beam optical tweezers optimized for biological studies. By high resolution, we mean sub-nanometer positional, femto-newton force and millisecond time resolution. We chose single-beam optical tweezers over the more stable dual-beam tweezers because of the design of the experiments conducted on the setup: surface-coupled assays. Such assays provide a large number of molecules on the flow cell surface. The interaction with these molecules can be quickly probed in a serial manner. This shortens the time needed to probe enough molecules for acquiring good statistics. The assembly of an experiment in a dual beam tweezers typically is more cumbersome and time consuming than pre-assembling many probes in parallel coupled to a surface. In addition, some biological experiments are only feasible in surface assays like measuring the stepping of a motor on a microtubule. We optimized the setup (i) by measuring the optimal filling ratio that maximizes the trapping efficiency and (ii) by implementing a temperature feedback to minimize drift that compromises the setup resolution.

To achieve the desired resolution, we identified, measured, and reduced the noise on the setup (Fig. 3.4). The low noise levels on the setup allowed for sub-nanometer measurements on a scale of 1 ms–100 s and reflected the effectiveness of the solutions utilized and thus we recommend: (a) a compact setup. This does not mean to lose any of the functionalities of the setup as demonstrated by our setup. (b) To keep the laser and the optics as close as possible to the optical table which helps in reducing the mechanical noise on the setup. This is in contrast to many protocols with laser heights of 100 mm

and higher [85]. (c) To use active vibration isolation systems. Such systems provide high damping performance and they are practical and easy to implement which makes the choice of where to build the setup within a building more flexible with respect to vibrational noise in the building. (d) As a diagnostic tool, we found that monitoring the temperature of different parts of the setup is beneficial. For example, by measuring the microscope temperature, we found that the microscope limited fast restoration of thermal equilibrium after a disturbance due to its long relaxation time constant.

To improve the throughput of the experiments, we motorized the setup and automated its calibration. Except for manual insertion of the sample, the whole setup is controlled via programming routines written in LabView. Thus, for operating the setup, the user does not need to be backed up with technical information. In addition, in case of a malfunction, safety routines intervene to prevent hardware damage.

We measured the trap stiffness as a function of the filling ratio for 0.5–2 μm microspheres and complemented the measurements by Mie theory calculations. We found that slighty under-filling the objective maximizes the use of the available laser power thus optimizing the trapping efficiency. In the lateral direction, the optimal filling ratio depended on the microsphere size while axially it was fixed and independent of microsphere size with an optimal ratio ≈ 1. Thus, the optimal filling ratio is a compromise between the lateral and axial direction. What the exact value for the optimal filling ratio is, may depend on the microsphere size, whether an oil or a water immersion objective is used, and how well the objective is corrected for the trapping laser wavelength. Based on our experiments and calculations, an under-filling ratio $\approx 0.9 \pm 0.05$ is a good compromise for a high-numerical aperture objective. A direct consequence of optimizing the trapping efficiency is the reduction of optical damage on biological samples. Also, under-filling reduces drift since in the case of overfilling, the truncated laser power leads to additional heating of the objective. The problem of maximizing the trap stiffness for optical tweezers is analogous to minimizing the extent of a laser focus while retaining the most power in case of confocal microscopy or other high-resolution scanning techniques using multi-photon excitation or stimulated emission depletion [86]. For these techniques, optimizing the filling ratio should also result in maximal performance for a given laser power.

To minimize drift on the setup, we implemented an active temperature feedback that stabilized the objectives' temperature with millikelvin precision and restored thermal equilibrium within 100 s after a disturbance such as closing the shutter. Compared to

available temperature stabilization solutions our feedback system is easier to implement and provided an improved precision of 1–2 orders of magnitude[1]. Using the feedback, it was possible to maintain sub-base pair resolution. In comparison to our approach, Carter et al. [84] used a position feedback system in a surface-coupled assay where a fiducial mark on the surface of the flow cell was tracked using a detection laser. Abbondanzieri et al. [17] used a dual beam optical tweezers in which all optics other than the microscope were enclosed in a box filled with helium instead of air to reduce density fluctuations that caused pointing instabilities on the trapping laser. Moffitt et al. [21] also used a dual beam optical tweezers where they detected the position of the two trapped microspheres. Because of the tethered molecule, the motion of the two microspheres is correlated. Symmetric, in phase motion reflects no change on the tether extension and can be rejected, thus, improving the resolution. A common feature of these approaches is an added complexity to the setup, higher costs and, in the case of dual traps, a lower throughput. While our approach does not suffer from such drawbacks it additionally allows to change the experiment temperature and to perform the experiments under the same temperature conditions independent of the time of the day or season. This is particularly important when studying biomolecules. Also, it is possible to quickly increase the temperature which can be used, for example, to switch temperature sensitive protein and fluorescence dyes. Other high-resolution microscopy techniques in particular ones that use high-power infrared lasers and/or scanning approaches, e.g. multi-photon excitation techniques or STED [88], should also benefit from a stabilized objective temperature.

In conclusion, we've presented the design and demonstration of a high-resolution, high-throughput optical tweezers suited for biological studies—and non-biological studies for that matter. We showed that noise on the setup can be reduced via simple, rather than complicated, solutions. For the troublesome thermal drift, we provided a solution that did not only reduce thermal drift but also offered additional functionalities. We also optimized the trapping efficiency with respect to the filling ratio and measured the lateral and axial trapping efficiency dependence on the microsphere size. At its current status, there is plenty of room for improving the setup. For instance, to utilize the ability of optical tweezers to exert and measure torque, to simultaneously measure rotations and displacements, and torques and forces [89, 90]. Additionally, it is possible to combine the setup with other single molecules techniques [91, 92]. In particular, total-internal reflection fluorescence microscopy (TIRF) that is ideal for surface assays. Finally, in

[1]Just recently, a commercial system with millikelvin precision became available [87].

the long run, full automization of the setup will be a significant improvement that will improve the productivity and promote using optical tweezers on a wider scale.

Chapter 7

Publications

- Mohammed Mahamdeh, Citlali Pérez Campos, and Erik Schäffer
  "Under-filling trapping objectives optimizes the use of the available laser power in optical tweezers", *Optics Express*, 19, 11759–11768 (2011) — Chapter 4

- Mohammed Mahamdeh and Erik Schäffer
  "Optical tweezers with millikelvin precision of temperature-controlled objectives and base-pair resolution", *Optics Express* 17, 17190–17199 (2009) — Chapter 5

  Also selected for: *The Virtual Journal of Biomedical Optics* Vol. 4, Iss.11 (2009)

Appendix A

Protocol for building high resolution optical tweezers

The following is the protocol used for building our setup. Parts of the protocol is specific for our setup but most of the protocol is general and applicable to other setups. When needed, Notes, control measurement suggestions, and warnings are put forward.

Note: Read the full protocol at least once before beginning your work.

Warning! Make sure to wear protection goggles designed for the used laser wavelength and maximum laser power.

Warning! Take off possible reflecting items like watches, rings,..etc. Also be ware of clothing with extension that can easily get into the laser path, for example, jackets and scarfs!

Warning! WEAR GLOVES. Optics are easy to contaminate and hard to clean.

Warning! The speed of applying the protocol is a matter of experience. Make sure to take breaks when feeling tired or out of focus.

Warning! Make sure that there is no open ends in the laser path especially when the laser width is small ($< 4\,mm$). During alignment, you can use a beam dump as the final

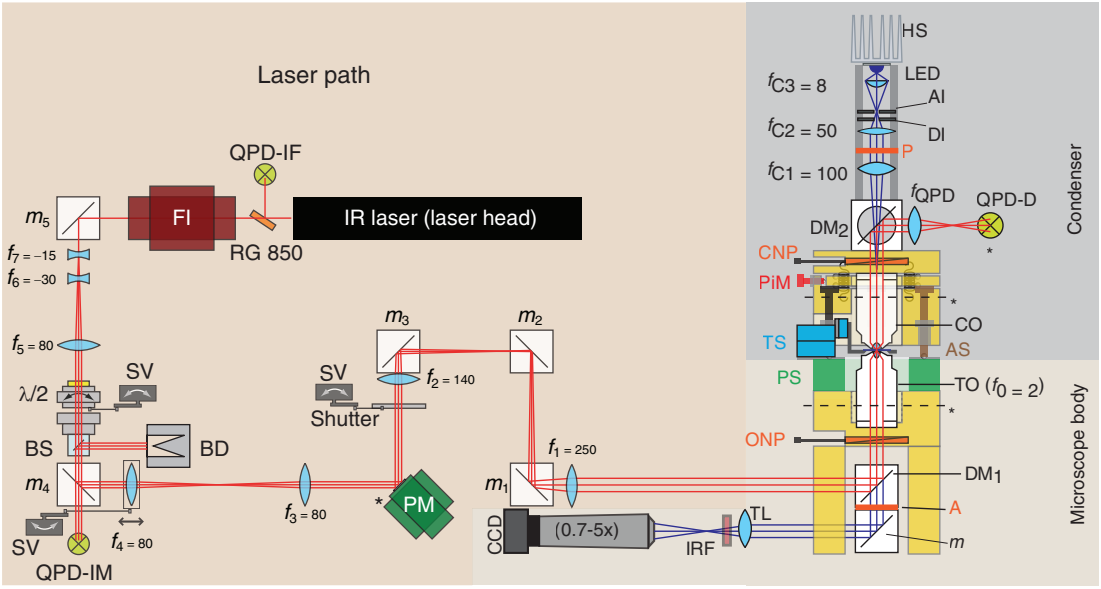

FIGURE A.1 OPTICAL TWEEZERS SCHEMATIC - Schematic drawing of the laser path (top view) and the microscope body and condenser (side view). Abbreviations are the same as those in Fig 3.6 and 3.9

piece in the laser path.

Note: For alignment purposes the laser power should be as low as possible. Set the laser power as low as possible but high enough to be detected by the used detection cards.

Tools needed

The following tools are required (Fig. A.2):

1. Alignment pinholes suitable for the mounting system used. We used the Microbench cage system (Mirobench, Linos, Germany). For pinholes, we used the 1 mm diameter pinholes from Thorlabs (CPA1, Thorlabs, Germany). The number of pinholes used varies depending on the alignment step but usually not less than two pinholes.

2. IR laser detection disk fixed onto a pinhole. We used a pinhole from Thorlabs (VRC4CPT, Thorlabs, Germany). From this point on, detection cards on pinholes are referred to as "detection pinholes".

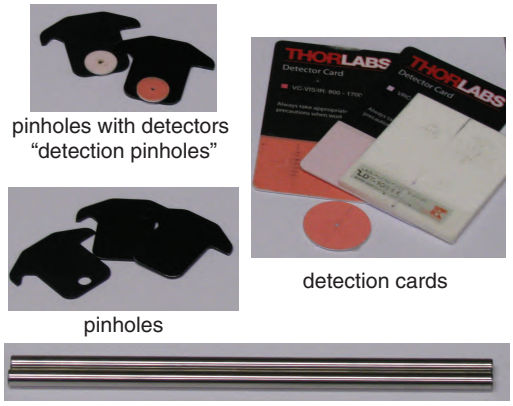

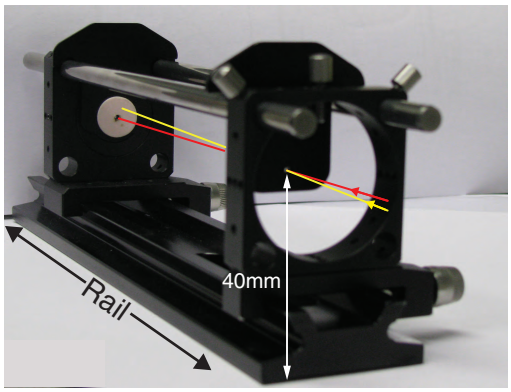

FIGURE A.2 ALIGNMENT TOOLS - photos of the tools needed for alignment plus an example of alignment. The red and yellow lines resembles the cases of an on-axis laser beam and a tilted laser beam, respectively.

3. Schematics of the setup printed on an A3 paper and fixed them on a wall nearby the setup.
4. Laser power meter (for high laser powers).
5. Auxiliary CCD camera for which the CCD chip position is known.

Warning! CCD cameras are quite sensitive to high intensity light. Even apparently low laser intensity can cause substantial damage to the CCD camera. Make sure to protect the camera with suitable filters.

A.1 Laser path alignment, I

This part covers the laser path from the laser head to the laser mirror m_4. At this point, the mounted parts should be: the base optical top, the spacer optical top, the pumping diode laser mounted on a heat sink that is fixed on the optical top and rails for the microbench mounting system.

Control: A good practice is to measure the laser power before and after inserting optics to the optical path. This is a fast and direct measurement of the transmission of the optics used. It also serves as a diagnostic tool in case the measured transmission is other than expected

1. Fix the laser head into the optical table. Make sure that the laser height is 40 mm above the optical table by using the detection pinhole. Pay attention that the optical fiber connecting the pumping diode and the laser head is firmly fixed on the optical table. It should not be stressed and it should not be in contact with other parts in the setup.

   Control: Laser pointing and power stability.

2. Insert the RG850 filter into the laser path at 45°. The RG850 will block any traces of the 808 nm pumping laser light. It will also reflect a certain amount from the 1064 nm trapping laser light. The reflected light is measured by the QPD-IF and is used as input for the intensity feedback.

   Control: Laser power stability with intensity feedback to assess the feedback improvement on stability.

3. Insert the Faraday Isolator. Make sure to follow the alignment protocol supplied by the manufacturer to gain optimal performance and minimum laser losses.

4. Insert the m_5 laser mirror.

5. *Galilean telescope*

   - Insert the first lens (f_7) of the 3 lens Galilean telescope.

     Note: Prior to inserting the rest of telescope lenses to the optical path, use a lens design software to calculate the separations between the lenses that corresponds to the desired magnification. Since we used Linos lenses, we used "Linos Photonics: Winlens3d basic"; a free design software offered by Linos, http://www.winlens.de/

     Control: Laser width measurement. Just before the first lens measure the laser profile width (ω_{before1}) using the knife-edge method [78]. This measurement is needed for measuring the magnification of the first telescope.

   - Insert the rest of the telescope lenses (f_6 and f_5). These lenses need to be fixed on adjustable x-y mounts to be able to move the lens perpendicular to the optical axis.

   - Adjust the separation between the lenses such that the laser emerges collimated from the telescope.

   - Adjust the x-y position of the lenses such that the laser emerges on axis from the telescope.

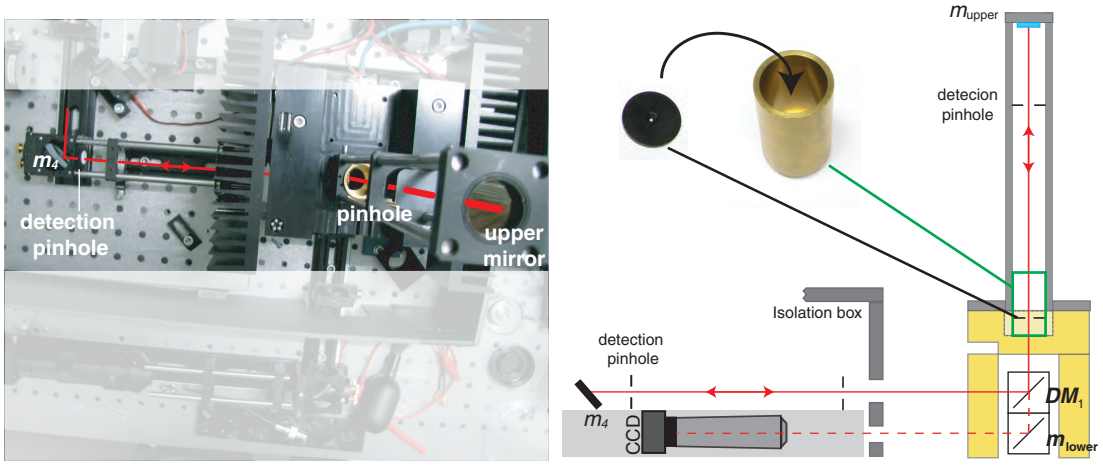

FIGURE A.3 LASER-MICROSCOPE ALIGNMENT

- Test the collimation of the laser by comparing the laser size directly after the telescope and at a distance >1 m away. Test whether the laser is on axis by using the pinholes.

  Control: First telescope magnification. Directly after the final lens of the telescope, measure the laser width(ω_{After1}) and calculate the magnification ($M_{\text{telescope1}} = \omega_{\text{After1}}/\omega_{\text{Before1}}$).

6. *Intensity control unit*. Insert the $\lambda/2$ wave plate and polarizing beam splitter (BS) into the laser path.The beam splitter should be fixed on a rotatable mount. Set the beam splitter at an angle such that the reflected light is directed into a beam dump (BD). To monitor the transmitted power, place a QPD (QPD-IM) or photodiode after m_4 (next step).

   Control: Beam splitter extension ratio measurement.

7. Insert m_4 laser mirror.

A.2 Laser-microscope alignment

The aim of this part is to align the microscope body relative to the laser. When the laser is reflected by the dichroic mirror (DM_1), the laser should be on axis of the trapping objective (Fig. A.3).

1. Using the pinholes, align the reflected laser from m_4.

2. Fix the dichroic mirror (DM_1) on its holder. The laser should hit the mirror at the center.

   Note: If differential interference microscopy is included in the setup then you need to add the analyzer between (DM_1) and the lower silver mirror (m_{lower}).

3. Insert the custom-made hollow cylinder in the microscope body in place of the trapping objective (TO). Insert the custom-made pinhole into the hollow cylinder (Fig. A.3).

4. Build a cage system around the cylinder 50 to 100 cm long with a mirror fixed at its end.

5. Adjust the position of the microscope body such that the laser beam traveling from $m_4 \rightarrow DM_1 \rightarrow m_{\text{upper}}$ will follow the same path when reflected from m_{upper}. Use the detection pinholes.

6. A minute part of the reflected laser passes through DM_1 (dashed red lines in Fig. A.3). Use the lower mirror (m_{lower}) to reflect the transmitted light to be on axis (check alignment using the pinholes).

7. Center the CCD+zoom relative to the laser light by imaging the laser onto the CCD image center. Check that the zoom is centered relative to the laser by changing the zoom while monitoring the laser spot. If the zoom is aligned properly, then the spot will stay centered regardless of the zoom factor.

   Note: Use the video routine (video.vi) to stream the CCD images. The routine has a centering function which is quite handy for alignment.

8. Remove the alignment cage (step 5) and insert the trapping objective (TO), the piezo stage (PS), the travelling stage (TS) and the tube lens (TL).

9. Apply a drop of immersion oil ($\approx 10-30\,\mu$l) and fix a clean cover slip on the sample holder. Adjust the axial position of the sample until a sharp image of the laser focus (an airy disk) is observed on the CCD. The image is due to the laser reflection at the glass-air interface. The 4% reflected laser light is more than sufficient to form an image on the CCD camera. Check that the image is still centered when changing the zoom factor as well as when moving the TL around its nominal position. If that is not the case check the alignment again (steps 5–7).

A.3 Laser path alignment, II

This part covers the laser path from m_4 to the microscope.

1. Block the laser just before the microscope. Take out TS, PS and TO.

2. *Axial control- part 1*. Fix f_4 into a movable lens mount and f_3 into an x-y adjustable mount. Adjust the position of the two lenses such that the laser emerges from the telescope collimated and on axis.

3. *Lateral control*. The piezo tilt mirror needs to be in the focal plane of the f_3.

   - take out f_4. f_3 focuses the beam in its back focal plane.

     Warnning! To avoid harming the camera by the focused laser light, lower the laser intensity using the intensity control unit

   - To precisely locate the back focal plane of f_3, use the auxiliary CCD camera and mark the plane position.
   - Replace the auxiliary CCD camera with the piezo tilt mirror (PM). Insert f_4 and check that the laser is collimated again.
   - Using the tilt adjustment screws on the piezo tilt mirror holder, adjust the static tilt of mirror so that the reflected laser is still on axis.

   Note: When adjusting the static tilt of the piezo mirror, the mirror should be operational and adjusted to its mid-range position.

4. *Kepler telescope*. The Kepler telescope expands the laser and images the piezo tilt into the back focal plane of TO as following:

   - Unblock the laser path.
   - Position the auxiliary CCD chip onto the focal plane of the objective.

     Note: The position of the back focal plane is provided by the objective manufacture.

   - Use the mirrors (m_{3-1}) to guide the laser to the microscope.

     Warnning! To avoid harming the camera by the focused laser light, lower the laser intensity using the intensity control unit

   - Insert f_1 and adjust its position such that the laser is focused onto the CCD camera (i.e. the back focal plane of TO)

- Block the laser light after f_1. Take out f_4 so the laser in focused on the tilt mirror. To make the tilt mirror be in a conjugate plane to the objective back focal plane, it should be positioned in the focal plane of f_2. Adjust the position of f_2 such that the laser emerges collimated.
- Insert f_4. If the distance between f_2 and f_1 is set correctly then the laser is collimated after f_1. If this is not the case, use the movable part of the U-shaped path (the arm between m_3 and m_2) to adjust the distance between the two lenses.

Control: Second telescope magnification. Measure the laser profile before f_2, ω_{befor2}, and after f_1, ω_{After1}, and calculate the magnification of the telescope ($M_{\text{telescope2}} = \omega_{\text{After2}}/\omega_{\text{Before2}}$). The final magnification $M_{\text{final}} = M_{\text{telescope1}} \times M_{\text{telescope2}}$ and the filling ratio of the objective $\alpha = \omega_{\text{after2}}/(2\text{NAf}_0)$.

Control: Check if the laser profile at f_2 is the same as at f_3.

5. Insert TO, PS and TS with the fixed slide on the holder.

6. *Axial control- part 2*. To adjust the axial position of the laser in the sample plane, f_4 is translated along its rail so to change the divergence of the beam. Misalignments on the f_4 rail leads to additional lateral movement and possible disturbances on the laser profile.

   - Translate f_4 to one end of the movable lens rail. Change the axial position of the sample to restore the image of the laser focus. It is likely that the laser is not on the center of image. Use f_5 or f_3 to center the laser in the image.
   - Translate f_4 to the other end. Center the laser as in the previous step.
   - Repeat the previous two steps until there is no lateral movement of the focus when f_4 is moved from one end to the other. We found that it is best to use one lens to adjust the lateral position of the laser. For example, when f_4 is moved to one end, we used f_3, and when moved to the other end, we used f_5 but not f_3 and f_5 at the same time.
   - Move the sample axially around the focal plane. If the building and collapsing of the focus is symmetric then there is no need for further adjustment. If not, use f_5 and f_6 to correct it.
   - If misalignment persists then correct it using m_1 and m_2; one mirror is used to center the focus and both are used to collimate the laser. When the laser

beam is collimated and centered then a symmetric airy pattern is observed when translating the sample axially around the focal plane.

A.4 The microscope

1. Prepare a flow cell made of two cover slides joined by a sticky tape and filled with nano-pure water. Take out the slide used in the previous protocol and fix the sample on the sample holder. Then apply another immersion oil drop on the upper slide.

2. Place the condenser on top of the microscope body. Take out the f_{QPD} lens and the detection QPD (QPD-D) from the detection arm in the microscope. Use the three adjustment screws (AS) to set the axial separation between the microscope body and the condenser so that the trapping and the condenser objectives are confocal which you check by reflecting the laser light after the condenser with the DM_2. Using a detection card, examine the laser beam size at the condenser and 1–3 m away.

3. Insert f_{QPD} and QPD-D. Make sure proper filters are in front of QPD-D. Remember that f_{QPD} is used to image the back focal plane of the condenser objective on the detection QPD. The focal length of f_{QPD} should be chosen such that the image of the back focal plane covers or exceeds the detection area of the QPD.

4. Turn on the LED. Adjust the illumination of the LED (via the applied voltage) to avoid saturating the CCD camera.

5. Use a Bertrand lens to image the back focal plane of the trapping objective and the condenser on the CCD. Align the condenser objective (CO) using the tiny pico motor (PiM); the two back focal planes should coincide.

6. To achieve Köhler illumination, adjust f_{C2} and f_{C3} so the LED and the aperture iris (AI) are imaged in the back focal plane of the condenser objective. Adjust the lateral position of the LED to center its image in the back focal plane of the condenser objective.

7. Remove the Bertrand lens and adjust the position of the diaphragm iris (DI) to image it in the sample plane. Adjust the DI laterally to center it in the image.

With the previous step, the mechanical construction of the optical tweezers is complete. To operate the setup, additional electronics and control software are needed (as mentioned in the Chapter 3).

Appendix B

Controls

Following are protocols for the controls recommended in the previous sections

B.1 Pointing and power stability

Please refer to schematic drawing, Fig. B.1

Tools

For this control you will need:

1. Laser mirror.
2. QPD.
3. Laser dump.
4. Tubes for enclosing the path between the laser and the QPD.
5. *x*-*y* adjustable lens mount.
6. Detection card.
7. Acquisition card and LabView software.
8. Data analysis software (e.g. OriginLab or MatLab®).

Note: For this protocol the room needs to equilibrate. Best is to setup the measurement apparatus then let the setup to equilibrate over night

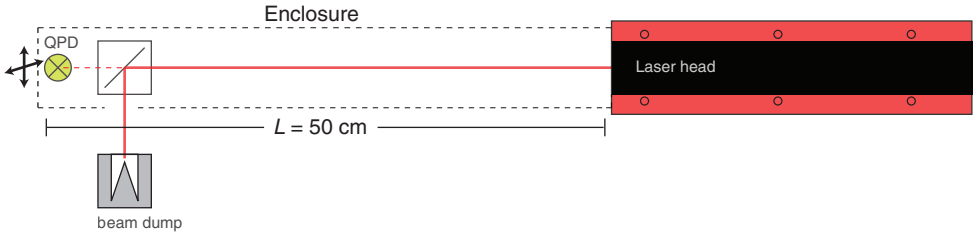

FIGURE B.1 POINTING AND POWER STABILITY CONTROL MEASUREMENT

Proceure

1. Place the laser mirror at 45° to the laser path.
2. Place the beam dump parallel to the mirror where the laser is supposed to be reflected.
3. Mount the QPD on the x-y adjustable mount and place it behind the laser mirror.
4. Use the tubes to enclose the path between the mirror and the laser head. Use tape to seal the contact points.
5. Turn on the laser and set it to the working power. At this stage the laser is very narrow and its intensity is quite high. Make sure to have the protective glasses on and the right detection card.
6. Check that the laser is being reflected from the mirror into the beam dump. If not use the adjustment screws of the mirrors.
7. Acquire the QPD signal for the three axes using the QPD.vi. The mirror has a reflectivity of 99.8 %. The transmitted light is enough for the measurement.
8. Align the QPD center relative to the laser using the adjustment screws on the mount. When aligned, the x and y signals are minimum.
9. Record the QPD signals with the following setting: 1 kHz acquisition rate for 1000 s.
10. Calibrate the QPD. The pointing stability is measured in radians (rad) while the QPD signal is in Volts. Thus, a conversion factor is needed.

    - Use the adjustment screws on the x-y mount to scan the laser across the QPD. Rotate the screw in steps of a quarter of a turn (90°, a full rotation is 250 μm

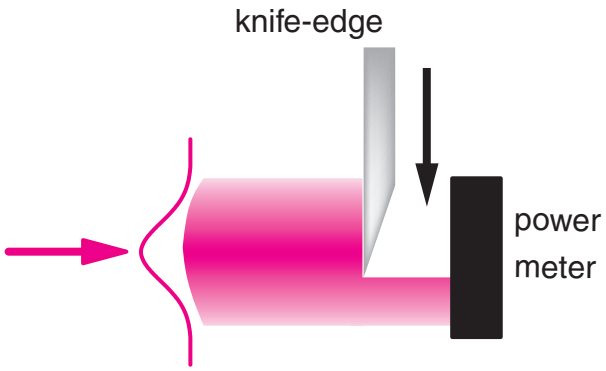

FIGURE B.2 LASER WIDTH MEASUREMENT

for our x-y mount, 14.202.0025, Owis, Germany). For every step measure the voltage. Scan the laser from the maximum voltage to the minimum voltage. Scan one axis at a time.

- Plot the voltage as a function the distance (rotations).
- Fit the data with a Boltzmann sigmoidal fit, $V = V_{max} + [(V_{min} - V_{max})/(1 + exp((x - x_0)/dx))]$ with x_0 and dx as fitting parameters. V_{min} and V_{max} can also be fit parameters. The slope of the fit is the volt-to-meter conversion factor, $C = (V_{min} - V_{max}/4dx)$
- Finally, the volt to radian conversion factor is $C_{rad} = C/L$
- With the conversion factor known. Analyze the laser pointing stability using the x and y QPD signals. Use the sum signal for power stability analysis.

B.2 Laser width measurement

This protocol measures the laser beam width. For a Gaussian beam, the width is the distance from the beam center to the point at which its intensity falls to $1/e^2$ (Fig. 4.1b)

Tools

For this protocol you will need the following:

1. Micrometer translation stage.

2. Razor blade with sharp, deformation-free edges.
3. Laser power meter.
4. Data analysis software (e.g. OriginLab or MatLab®).

Procedure

1. Fix the razor blade on the micrometer translation stage.
2. Fix the stage such that the razor blade is perpendicular to the direction of propagation of the collimated, on-axis beam. Make sure that the blade is not blocking any of the laser beam, at least at this stage.
3. Use the detector to measure the laser power.
4. Using the stage move the blade in steps of 62.5 μm (one quarter of a a full turn for the stage we used) and record the measured laser power.

   Note: The higher the number of steps the more accurate the measurements. We found that 20 steps is a good compromise between accuracy and measurement time. More steps caused no significant change on the beam width precision.
5. Plot the laser power as a function of the blade displacement. Fit the data with an error function:

$$P(x) = \frac{P_0}{2}\left(1 + erf(\frac{\sqrt{2}(x - x_0)}{\omega_0})\right) \tag{B.1}$$

   where $P(x)$ is the measured power, P_0 is the total power, $erf(x)$ is the error function, x_0 is the beam center position, x is the blade displacement and ω_0 is the beam width. The error function is defined as:

$$efr(x) = \frac{2}{\sqrt{\pi}}\int_0^x \exp(-u^2)\mathrm{d}u. \tag{B.2}$$

B.3 Beam splitter extension ratio

The extension ratio of the beam splitter (BS) used in the intensity unit defines the maximum and the minimum power in the focus of the trapping objective.

Tools

1. Laser power meter.

2. $\lambda/2$ wave plate.
3. Beam splitter.

Procedure

1. Take out BS and measure the laser power.
2. Insert BS and rotate the wave plate until the power is at its maximum.
3. Rotate the wave plate until the power is at its minimum.
4. The extension ratio of BS is ER = minumum power/ maximum power.

Glossary

$< x^2 >$	mean squared displacement
α	electrical dipole moment- Chapter 2
α	filling ratio- Chapter 4
β	displacement sensitivity
$\Delta\theta$	tilt mirror angular range
ΔF_{rms}	force rms noise
Δr	lateral range of the focus in the sample plane
Δx	displacement of the microsphere relative to the trap center
Δx_{rms}	positional rms noise
Δz	axial range of the focus in the sample
$\Delta_{movable}$	movable lens travel range
ϵ_0	vacuum dielectric constant
γ	frictional drag coefficient
κ	trap stiffness
κ_t	tether stiffness
λ	trapping laser wavelength in vacuum
ν	drag velocity
ω_0	laser width at $1/e^2$
$\sigma_x(\tau)$	Allan deviation

τ_c	correlation time constant
τ_m	microscope thermal relaxation time constant
τ_o	objective thermal relaxation time constant
$\mathbf{E}$	electrical field
θ_i	angle of incidence
θ_r	angle of refraction
c	speed of light in vacuum
D	diffusion coefficient
D_v	diffusion coefficient measured in V^2/s
D_0	back aperture diameter
D_{H_1}	principle plane diameter
D_{NA}	exit pupil diameter
D_{opt}	optimal filling ratio
E	electrical field magnitude
f	frequency
f	objective focal length - Chapter 4
F_d	drag force
f_s	sampling frequency
f_c	corner frequency of a power spectral density
F_{grad}	gradient force
F_{scat}	scattering force
f_{stage}	stage frequency
I	laser intensity in the focus
k	wave number
k_B	Boltzmann constant, 1.38×10^{-23}J/K
m	relative refractive index
N	number of measurements

n	refractive index
N_e	effective number of measurements; number of uncorrelated measurements
n_m	refractive index of the medium
n_{PS}	refractive index of polystyrene
n_p	refractive index of the microsphere
P	laser power in the focus
$P(f)$	power spectral density
P_{trunc}	power normalization factor to account for power loss due to truncation
R	reflectance
r	microsphere radius
r	radial coordinate - Chapter 4
S_0	plateau value from the Lorentzian fit
T	absolute temperature
T	objective transmission- Chapter 4
T	transmittance- Chapter 2
t_m	measurement time
3D	three dimensional
CCD	charged-coupled device
COV	coefficient of variation
DIC	differential interference contrast
dsDNA	double stranded DNA
EMI	electromagnetic interference
GMLT	generlaized Mie-Lorenz theory
IR	infrared
KCL	potassium chloride
LED	light emitting diode
M^2	beam quality factor

NA numerical aperture

PID proportional-integral-derivative feedback

PSD power spectral density

QPD quadrant photodiode

rms root mean square

TMV Tobacco mosaic virus

List of Figures

References

[1] Ashkin, A. History of optical trapping and manipulation of small-neutral particle, atoms, and molecules. *IEEE J. Sel. Top. Quant.* **6**, 841 –856 (2000).

[2] Ashkin, A. Acceleration and trapping of particles by radiation pressure. *Phys. Rev. Lett.* **24**, 156–159 (1970).

[3] Ashkin, A. & Dziedzic, J. M. Optical levitation by radiation pressure. *Appl. Phys. Lett.* **19**, 283–285 (1971).

[4] Ashkin, A., Dziedzic, J. M., Bjorkholm, J. E. & Chu, S. Observation of a single-beam gradient force optical trap for dielectric particles. *Opt. Lett.* **11**, 288 (1986).

[5] Greenleaf, W. J., Woodside, M. T. & Block, S. M. High-resolution, single-molecule measurements of biomolecular motion. *Annu. Rev. Biophys. Biomol. Struct.* **36**, 171–190 (2007).

[6] Mehta, A. D., Rief, M., Spudich, J. A., Smith, D. A. & Simmons, R. M. Single-molecule biomechanics with optical methods. *Science* **283**, 1689–1695 (1999).

[7] Gutsche, C. *et al.* Micro-rheology on (polymer-grafted) colloids using optical tweezers. *J. Phy: Cond. Matt.* **23**, 184114 (2011).

[8] Mitchem, L. & Reid, J. P. Optical manipulation and characterisation of aerosol particles using a single-beam gradient force optical trap. *Chem. Soc. Rev.* **37**, 756–769 (2008).

[9] Ashkin, A. & Dziedzic, J. Optical trapping and manipulation of viruses and bacteria. *Science* **235**, 1517–1520 (1987).

[10] Ashkin, A., Schütze, K., Dziedzic, J. M., Euteneuer, U. & Schliwa, M. Force generation of organelle transport measured in vivo by an infrared laser trap. *Nature* **348**, 346–348 (1990).

[11] Zhang, H. & Liu, K.-K. Optical tweezers for single cells. *J. R. Soc. Interface* **5**, 671–690 (2008).

[12] Svoboda, K., Schmidt, C. F., Schnapp, B. J. & Block, S. M. Direct observation of kinesin stepping by optical trapping interferometry. *Nature* **365**, 721–727 (1993).

[13] Veigel, C. & Schmidt, C. F. Moving into the cell: single-molecule studies of molecular motors in complex environments. *Nat. Rev. Mol. Cell. Biol.* **12**, 163–176 (2011).

[14] Bormuth, V., Varga, V., Howard, J. & Schäffer, E. Protein friction limits diffusive and directed movements of kinesin motors on microtubules. *Science* **325**, 870–873 (2009).

[15] Seol, Y., Li, J., Nelson, P., Perkins, T. T. & Betterton, M. D. Elasticity of short DNA molecules: theory and experiment for contour lengths of 0.6-7 μm. *Biophys. J.* (2007).

[16] Bustamante, C., Bryant, Z. & Smith, S. B. Ten years of tension: single-molecule DNA mechanics. *Nature* **421**, 423–427 (2003).

[17] Abbondanzieri, E. A., Greenleaf, W. J., Shaevitz, J. W., Landick, R. & Block, S. M. Direct observation of base-pair stepping by RNA polymerase. *Nature* **438**, 460–465 (2005).

[18] Wang, M. D., Yin, H., Landick, R., Gelles, J. & Block, S. M. Stretching DNA with optical tweezers. *Biophys. J.* **72**, 1335–1346 (1997).

[19] Pralle, A., Prummer, M., Florin, E. L., Stelzer, E. H. & Hörber, J. K. Three-dimensional high-resolution particle tracking for optical tweezers by forward scattered light. *Microsc. Res. Tech.* **44**, 378–386 (1999).

[20] Gittes, F. & Schmidt, C. F. Thermal noise limitations on micromechanical experiments. *Eur. Biophys. J.* **27**, 75–81 (1998). 10.1007/s002490050113.

[21] Moffitt, J. R., Chemla, Y. R., Izhaky, D. & Bustamante, C. Differential detection of dual traps improves the spatial resolution of optical tweezers. *Proc. Natl. Acad. Sci. U S A* **103**, 9006–9011 (2006).

[22] Schäffer, E., Tolić-Nørrelykke, S. F. & Howard, J. Surface forces and drag coefficients of microspheres near a plane surface measured with optical tweezers. *Langmuir* (2007).

[23] Carter, A. R. *et al.* Stabilization of an optical microscope to 0.1 nm in three dimensions. *Appl. Opt.* **46**, 421–427 (2007).

[24] Ashkin, A. Forces of a single-beam gradient laser trap on a dielectric sphere in the ray optics regime. *Biophys. J.* **61**, 569–582 (1992).

[25] Harada, Y. & Asakura, T. Radiation forces on a dielectric sphere in the Rayleigh scattering regime. *Opt. Comm.* **124**, 529 – 541 (1996).

[26] Khlebtsov, N. G. Methods for calculating light scattering by single particles. Retrieved from http://www.astro.spbu.ru/DOP/3-REVS/khleb1e.ps (2011).

[27] van de Hulst, H. *Light scattering by small particles* (Dover Puplications Inc., 1981).

[28] Sheppard, C. J. R. High-aperture beams. *J. Opt. Soc. Am. A* **18**, 1579–1587 (2001).

[29] Urey, H. Spot size, depth-of-focus, and diffraction ring intensity formulas for truncated Gaussian beams. *Appl. Opt.* **43**, 620–625 (2004).

[30] Mahajan, V. N. Uniform versus Gaussian beams: a comparison of the effects of diffraction, obscuration, and aberrations. *J. Opt. Soc. Am. A* **3**, 470–485 (1986).

[31] Mazolli, A., Neto, P. A. M. & Nussenzveig, H. M. Theory of trapping forces in optical tweezers. *Proc. R. Soc. Lond. A* **459**, 3021–3041 (2003).

[32] Dutra, R. S., Viana, N. B., Neto, P. A. M. & Nussenzveig, H. M. Polarization effects in optical tweezers. *J. Opt. A-Pure Appl. Opt.* **9**, S221 (2007).

[33] Lock, J. A. Calculation of the radiation trapping force for laser tweezers by use of generalized Lorenz-Mie theory. I. localized model description of an on-axis tightly focused laser beam with spherical aberration. *Appl. Opt.* **43**, 2532–2544 (2004).

[34] Lock, J. A. Calculation of the radiation trapping force for laser tweezers by use of generalized Lorenz-Mie theory. II. on-axis trapping force. *Appl. Opt.* **43**, 2545–2554 (2004).

[35] Nieminen, T. A. *et al.* Optical tweezers computational toolbox. *J. Opt. A-Pure Appl. Opt.* **9**, S196 (2007).

[36] Nieminen, T. A., Rubinsztein-Dunlop, H. & Heckenberg, N. R. Calculation of the T-matrix: general considerations and application of the point-matching method. *JQSRT* **79-80**, 1019 – 1029 (2003).

[37] Nieminen, T. A., Rubinsztein-Dunlop, H. & Heckenberg, N. R. Multipole expansion of strongly focussed laser beams. *JQSRT* **79-80**, 1005 – 1017 (2003).

[38] Berg-Sørensen, K. & Flyvbjerg, H. Power spectrum analysis for optical tweezers. *Rev. Sci. Instrum.* **75**, 594–612 (2004).

[39] Eggert, H. & Mameren, J. V. Sptial and temporal resolution of optical tweezers. Retrieved from http://www.jpk.com/optical-tweezers.233.html (2011).

[40] Gibson, G. M., Leach, J., Keen, S., Wright, A. J. & Padgett, M. J. Measuring the accuracy of particle position and force in optical tweezers using high-speed video microscopy. *Opt. Express* **16**, 14561–14570 (2008).

[41] Czerwinski, F., Richardson, A. C. & Oddershede, L. B. Quantifying noise in optical tweezers by Allan variance. *Opt. Express* **17**, 13255–13269 (2009).

[42] Moffitt, J. R., Chemla, Y. R., Smith, S. B. & Bustamante, C. Recent advances in optical tweezers. *Annu. Rev. Biochem.* **77**, 205–228 (2008).

[43] Gittes, F. & Schmidt, C. F. Signals and noise in micromechanical measurements. *Methods Cell Biol.* **55**, 129–156 (1998).

[44] CVI Melles Griot. Fundamentals of vibration isolation. Retrieved from https://www.cvimellesgriot.com/Company/CoolTips.aspx (2011).

[45] Neuman, K. C. & Block, S. M. Optical trapping. *Rev. Sci. Instrum.* **75**, 2787–2809 (2004).

[46] Technical Manufacturing Corporation. Technical background. Retrieved from http://www.techmfg.com/techbkgd/intro.htm (2011).

[47] Accurion gmbh. principles of halcyonics active vibration isolation technology. Retrieved from http://www.halcyonics.de/technology (2011).

[48] Herzan LLC. Choosing a vibration isolation system. Retrieved from http://www.herzan.com/choosesystemA.html (2011).

[49] National Instruments. Avoiding ground loops. Retrieved from http://zone.ni.com/devzone/cda/tut/p/id/3035 (2011).

[50] Liu, Y. *et al.* Evidence for localized cell heating induced by infrared optical tweezers. *Biophys. J.* **68**, 2137–2144 (1995).

[51] Peterman, E. J. G., Gittes, F. & Schmidt, C. F. Laser-induced heating in optical traps. *Biophys. J.* **84**, 1308–1316 (2003).

[52] Liang, H. *et al.* Wavelength dependence of cell cloning efficiency after optical trapping. *Biophys. J.* **70**, 1529–1533 (1996).

[53] Neuman, K. C., Chadd, E. H., Liou, G. F., Bergman, K. & Block, S. M. Characterization of photodamage to Escherichia coli in optical traps. *Biophys. J.* **77**, 2856–2863 (1999).

[54] Svoboda, K. & Block, S. M. Biological applications of optical forces. *Annu. Rev. Biophys. Biomol. Struct.* **23**, 247–285 (1994).

[55] Paschotta, R. In encyclopedia of laser physics and tehcnology. Retrieved from http://www.rp-photonics.com/encyclopedia.html (2011).

[56] Fällman, E. & Axner, O. Design for fully steerable dual-trap optical tweezers. *Appl. Opt.* **36**, 2107–2113 (1997).

[57] Reihani, S. N. S. & Oddershede, L. B. Optimizing immersion media refractive index improves optical trapping by compensating spherical aberrations. *Opt. Lett.* **32**, 1998–2000 (2007).

[58] Denk, W. & Webb, W. W. Optical measurement of picometer displacements of transparent microscopic objects. *Appl. Opt.* **29**, 2382–2391 (1990).

[59] Allersma, M. W., Gittes, F., deCastro, M. J., Stewart, R. J. & Schmidt, C. F. Two-dimensional tracking of ncd motility by back focal plane interferometry. *Biophys. J.* **74**, 1074–1085 (1998).

[60] Dreyer, J. K., Berg-Sørensen, K. & Oddershede, L. Improved axial position detection in optical tweezers measurements. *Appl. Opt.* **43**, 1991–1995 (2004).

[61] Huisstede, J., van der Werf, K., Bennink, M. & Subramaniam, V. Force detection in optical tweezers using backscattered light. *Opt. Express* **13**, 1113–1123 (2005).

[62] Sischka, A. *et al.* Single beam optical tweezers setup with backscattered light detection for three-dimensional measurements on DNA and nanopores. *Rev. Sci. Instrum.* **79**, 063702 (2008).

[63] Berg-Sørensen, K., Oddershede, L., Florin, E.-L. & Flyvbjerg, H. Unintended filtering in a typical photodiode detection system for optical tweezers. *J. Appl. Phys.* **93**, 3167–3176 (2003).

[64] Bormuth, V., Howard, J. & Schäffer, E. LED illumination for video-enhanced DIC imaging of single microtubules. *J. Microsc.* **226**, 1–5 (2007).

[65] Mehta, S. B. & Sheppard, C. J. Partially coherent image formation in differential interference contrast (DIC) microscope. *Opt. Express* **16**, 19462–19479 (2008).

[66] Otto, O., Gutsche, C., Kremer, F. & Keyser, U. F. Optical tweezers with 2.5 kHz bandwidth video detection for single-colloid electrophoresis. *Rev. Sci. Instrum.* **79**, 023710 (2008).

[67] Keen, S., Leach, J., Gibson, G. & Padgett, M. J. Comparison of a high-speed camera and a quadrant detector for measuring displacements in optical tweezers. *J. Opt. A-Pure Appl. Opt.* **9**, S264 (2007).

[68] Huhle, A. & Seidel, R. Private communication (2011).

[69] Visscher, K. & Block, S. M. Versatile optical traps with feedback control. *Methods Enzymol.* **298**, 460–489 (1998).

[70] Tolić-Nørrelykke, S. F. *et al.* Calibration of optical tweezers with positional detection in the back focal plane. *Rev. Sci. Instrum.* **77**, 103101 (2006).

[71] Simpson, N. B., McGloin, D., Dholakia, K., Allen, L. & Padgett, M. J. Optical tweezers with increased axial trapping efficiency. *J. Mod. Opt.* **45**, 1943–1949 (1998).

[72] Bormuth, V. *et al.* Optical trapping of coated microspheres. *Opt. Express* **16**, 13831–13844 (2008).

[73] Jannasch, A. *et al.* Coated microspheres as enhanced probes for optical trapping. vol. 7038, 70382B (SPIE, 2008).

[74] Kim, H.-I. *et al.* Dependence of the optical trapping efficiency on the ratio of the beam radius-to-the aperture radius. *J. Korean. Phys. Soci.* **43**, 348–351 (2003).

[75] Bing-Huan, M. *et al.* Improvement of transverse trapping efficiency of optical tweezers. *Chin. Phys. Lett.* **25**, 2300 (2008).

[76] Samadi, A. & Reihani, N. S. Optimal beam diameter for optical tweezers. *Opt. Lett.* **35**, 1494–1496 (2010).

[77] Viana, N. B., Rocha, M. S., Mesquita, O. N., Mazolli, A. & Neto, P. A. M. Characterization of objective transmittance for optical tweezers. *Appl. Opt.* **45**, 4263–4269 (2006).

[78] Skinner, D. R. & Whitcher, R. E. Measurement of the radius of a high-power laser beam near the focus of a lens. *J. Phys. E: Sci. Instrum.* **5**, 237 (1972).

[79] Hell, S., Reiner, G., Cremer, C. & Stelzer, E. H. K. Aberrations in confocal fluorescence microscopy induced by mismatches in refractive index. *J. Microsc. 391–405* **169**, 391—-405 (1993).

[80] Rohrbach, A. Stiffness of optical traps: quantitative agreement between experiment and electromagnetic theory. *Phys. Rev. Lett.* **95**, 168102 (2005).

[81] Mahamdeh, M. & Schäffer, E. Optical tweezers with millikelvin precision of temperature-controlled objectives and base-pair resolution. *Opt. Express* **17**, 17190–17199 (2009).

[82] Moffitt, J. R. *et al.* Intersubunit coordination in a homomeric ring atpase. *Nature* **457**, 446–450 (2009).

[83] Mao, H., Arias-Gonzalez, J. R., Smith, S. B., Tinoco, I. & Bustamante, C. Temperature control methods in a laser tweezers system. *Biophys. J.* **89**, 1308–1316 (2005).

[84] Carter, A. R., Seol, Y. & Perkins, T. T. Precision surface-coupled optical-trapping assay with one-basepair resolution. *Biophys. J.* **96**, 2926–2934 (2009).

[85] Lee, W. M., Reece, P. J., Marchington, R. F., Metzger, N. K. & Dholakia, K. Construction and calibration of an optical trap on a fluorescence optical microscope. *Nat Protoc* **2**, 3226–3238 (2007).

[86] Pawley, J. B. (ed.) *Handbook of Biological Confocal Microscopy* (Plenum Press, New York, 1995).

[87] Belektronig GbR. HAT Control-B. http://www.belektronig.de (2011).

[88] Hell, S. W. & Wichmann, J. Breaking the diffraction resolution limit by stimulated emission: stimulated-emission-depletion fluorescence microscopy. *Opt. Lett.* **19**, 780–782 (1994).

[89] Gutiérrez-Medina, B., Andreasson, J. O. L., Greenleaf, W. J., Laporta, A. & Block, S. M. An optical apparatus for rotation and trapping. *Methods Enzymol* **475**, 377–404 (2010).

[90] La Porta, A. & Wang, M. D. Optical torque wrench: Angular trapping, rotation, and torque detection of quartz microparticles. *Phys. Rev. Lett.* **92**, 190801 (2004).

[91] Comstock, M. J., Ha, T. & Chemla, Y. R. Ultrahigh-resolution optical trap with single-fluorophore sensitivity. *Nat Methods* **8**, 335–340 (2011).

[92] Ishijima, A. *et al.* Simultaneous observation of individual atpase and mechanical events by a single myosin molecule during interaction with actin. *Cell* **92**, 161–171 (1998).

Acknowledgements

I would like to express my gratitude to Dr. Erik Schäffer for giving me the chance to do my studies in his group. I thank him for his tolerance, patience, encouragement and for teaching me all what I know about optical tweezers. Danke schön Erik.

I thank my TAC members: Prof. Jonathan Howard and Prof. Frank Jülicher for their advice and support.

Special thanks to the wonderful people of the nanomechanics group: Marcel Ander (for lending me some of his expertise and for the scientific and non-scientific discussions), Anita Jannasch, Anastasiya Trushko, Adrian Wichmann (for being Adrian), Avin Ramaiya, Deepikaa Menon, Michael Bugiel (Mr. Cool), Frederic Schiemann (for sharing the passion for football), and the new comers Christine Kiefer, Tobias Jachowski and Steve Simmert. Guys! It has been a pleasure working with you.

Thanks to the Howard lab for hosting me during the first two months of my work. Especially, former members: Dr. Volker Bormuth and Henning Urban.

I thank Nicholas Luzzietti for being a true friend and for proof reading parts of this thesis. Mehdi Damaghi, João Nunes, Avin Ramaiya, Adrian Wichmann, Frederic Schiemann, Martin Stewart and Tanuj Sapra for the joyful dinners, barbecues, discussions and much more.

Thanks to Hergen Brutzer, Daniel Klaue, Dominik Kauert for always helping me, answering my questions and for sharing sports activities.

Thanks to the table-soccer gang: Grzegorz Chwastek, Erdinc Sezgin, Dr. Jörg Mütze, Christoph Herold, Erdinc Sezgin, Dr. Thomas Weidemann, Senthil Arumugam and Jens Ehrig for the exciting, stress-relieving games.

I would also like to thank the PhD and the international office of the Dresden international graduate school for biomedicine and bioengineering, in particular Carolyn Fritzsche for her help in organizing my stay in Dresden.

أَخِيرًا و ليس آخرًا، اَلشّكر الجزِيل لعَائِلتِي الحبِيبة و أصدقَاء الأَعزَّاء. لو أنّ جلّ مَا أجد من هذَا العمل إبتسَامة رضىً منكم لكفت.